Research article

Published Online First

https://doi.org/10.1144/jgs2020-142

Magnitude, timing, and rate of slip along the Atacama fault system, northern Chile: implications for Early Cretaceous slip partitioning and plate convergence



N.M. Seymour^{1*}, J.S. Singleton¹, R. Gomila^{2,3}, S.P. Mavor¹, G. Heuser², G. Arancibia², S. Williams¹ and D.F. Stockli⁴

- Department of Geosciences, Colorado State University, 1482 Campus Delivery, Fort Collins, CO 80523, USA
- ² Departamento de Ingeniería Estructural y Geotécnica, Pontificia Universidad Católica de Chile, Santiago, Chile
- ³ Dipartimento di Geoscienze, Università degli Studi di Padova, Via G. Gradenigo n.6, Padova, Italy
- Department of Geological Sciences, The University of Texas at Austin, 2305 Speedway Stop C1160, Austin, TX 78712, USA
 NMS, 0000-0003-0040-063X; RG, 0000-0001-5807-2769; SPM, 0000-0002-3174-8148; GH, 0000-0001-5473-7356;
 GA, 0000-0003-2860-1302; SW, 0000-0001-6875-398X; DFS, 0000-0001-7652-2129
- * Correspondence: nseymour@stanford.edu

Abstract: Displacement estimates along the Atacama fault system (AFS), a crustal-scale sinistral structure that accommodated oblique convergence in the Mesozoic Coastal Cordillera arc, vary widely due to a lack of piercing points. We map the distribution of plutons and mylonitic deformation along the northern c. 70 km of the El Salado segment and use U–Pb geochronology to establish the slip history of the AFS. Along the eastern branch, mylonitic fabrics associated with the synkinematic c. 134–132 Ma Cerro del Pingo Complex are separated by 34–38 km, and mylonites associated with a synkinematic c. 120–119 Ma tonalite are separated by 20.5–26 km. We interpret leucocratic intrusions to be separated across the western branch by c. 16–20 km, giving a total slip magnitude of c. 54 ± 6 km across the El Salado segment. Kinematic indicators consistently record sinistral shear, and zircon (U–Th)/He data suggest dip-slip motion was insignificant. Displacement occurred between c. 133–110 Ma at a slip rate of c. 2.1–2.6 km Myr $^{-1}$. This slip rate is low compared to modern intra-arc strike-slip faults, suggesting (1) the majority of lateral slip was accommodated along the slab interface or distributed through the forearc or (2) plate convergence rates/obliquity were significantly lower than previously modeled.

Supplementary material: Full U-Pb, (U-Th)/He, petrographic, and structural data with locations is available at https://doi.org/10.6084/m9.figshare.c.5262177

Thematic collection: This article is part of the Isotopic dating of deformation collection available at: https://www.lyellcollection.org/cc/isotopic-dating-of-deformation

Received 20 July 2020; revised 8 December 2020; accepted 7 January 2021

Plate motion across most subduction zones is oblique (>22° from normal to the plate boundary) and partitioned between slab underthrusting and upper-plate lateral transport (Jarrard 1986; Woodcock 1986). Lateral transport of forearc slivers may be achieved through oblique underthrusting or partitioned between underthrusting, distributed forearc deformation, and/or along crustal-scale strike-slip faults (Fitch 1972; Beck 1983). Strike-slip faults dominate at margins where interplate coupling between a subducting oceanic slab and overriding continental plate is strong (Fitch 1972; Jarrard 1986). While the dynamics of oblique convergence have been well studied from a modeling perspective (e.g. Platt 1993; Tikoff and Teyssier 1994; Teyssier *et al.* 1995; Schütt and Whipp 2020), relatively few studies have provided detailed slip histories of intra-arc strike-slip fault systems in the upper plate of a subduction zone.

The regional tectonic history of an area is of foremost importance when studying oblique convergence, as changes in convergence angles over time will directly affect the distribution of strain (e.g. Scheuber *et al.* 1994). In particular, the absolute motion of the overriding plate with respect to the trench – which includes the magnitude and rate of slip along trench-parallel strike-slip faults – must be known to understand subduction zone processes such as slip partitioning (Jarrard 1986). There are significant variations and uncertainties in estimates of slip partitioning from modern subduction zones based on geodesy and strain modeling. For

example, the Median Tectonic Line of Japan accommodates c. 25% trench-parallel motion (Loveless and Meade 2010), the Liquiñe-Ofqui fault system of southern Chile accommodates c. 75% of modern trench-parallel motion (Wang et al. 2007), and the Sumatran fault system accommodates c. 33% to c. 66% of trenchparallel motion with the 40% of interseismic trench-parallel motion accommodated by distributed deformation within the subducting oceanic plate (Tikoff and Teyssier 1994; McCaffrey et al. 2000; Bradley et al. 2017). While active slip partitioning on modern intraarc strike-slip faults may be known from geodesy, these major structures have poorly constrained total displacement estimates and geologic (megayear-scale) slip rates. Detailed slip histories on these modern systems are hindered by a lack of exposure, as structures such as the Sumatran fault and Liquiñe-Ofqui fault system are in heavily vegetated areas where clear bedrock piercing points are difficult to identify. Although direct slip rates on fossil fault systems cannot be gleaned from geodetic data, erosion to deeper levels can expose piercing points, and the identification of crosscutting relationships marking the relative timing of slip along a fault system can be used to estimate slip rates.

The Atacama fault system (AFS), one of the best and most accessible examples of an exhumed major intra-arc fault system, runs for c. 1000 km through the Coastal Cordillera in northern Chile (Fig. 1). The AFS is a sinistral strike-slip, trench-linked structure that formed as a result of slip partitioning during Mesozoic SE-

directed oblique subduction (Scheuber and Andriessen 1990; Brown *et al.* 1993). Unparalleled exposure and the presence of pre-, syn- and post-tectonic intrusions cutting both brittle and ductile features along the AFS provide an excellent opportunity to reconstruct slip history. Previous estimates of slip along this system are poorly constrained because no clear piercing points have been identified across the fault system (Brown *et al.* 1993; Grocott and Taylor 2002). Using detailed geologic mapping, we identify offset markers along the AFS and use crosscutting relationships, geo-/thermochronology and geochemistry to provide robust constraints on the timing, magnitude and rate of slip along the El Salado segment of the AFS. We compare these data to slip rates and partitioning estimates from other major intra-arc strike-slip faults to understand the role of the AFS in accommodating oblique subduction.

Geologic setting

Atacama fault system

Mesozoic SE-directed subduction of the Aluk (Phoenix) plate below the north-south-trending South American plate margin produced a long-lived period of arc magmatism now preserved in the Coastal Cordillera (Scheuber and Andriessen 1990; Dallmeyer et al. 1996; Scheuber and González 1999; Parada et al. 2007). Lateral strain from the obliquely descending slab was partitioned between the subducting plate and overriding South American plate along the sinistral AFS, which is exposed in the Late Jurassic to Early Cretaceous magmatic arc for c. 1000 km between Iquique (20.5°S) and La Serena (30°S) (e.g. Naranjo et al. 1984; Scheuber and Andriessen 1990; Brown et al. 1993; Grocott et al. 1994; Scheuber et al. 1995; Grocott and Taylor 2002). The timing of AFS deformation has been tied to Coastal Cordillera magmatism and is broadly constrained to c. 140–110 Ma by crystallization and cooling ages of Coastal Cordillera granitoids (Grocott et al. 1994; Scheuber et al. 1995; Dallmeyer et al. 1996; Ruthven et al. 2020; Seymour et al. 2020).

The AFS is comprised of three distinct fault segments: the northern Salar del Carmen, central Paposo, and southern El Salado segment (e.g. Naranjo et al. 1984; Scheuber and Andriessen 1990; Brown et al. 1993; Grocott and Taylor 2002, Fig. 1). The Paposo and El Salado segments record a progression from ductile (mylonitic) to brittle strain (e.g. Scheuber and Andriessen 1990; Brown et al. 1993; Ruthven et al. 2020; Seymour et al. 2020). Studies of deformation along the Paposo segment document steeply dipping sinistral strike-slip duplexes developed in a transfensional regime near Antofogasta at c. 24°S (Cembrano et al. 2005; Veloso et al. 2015) and steeply dipping sinistral mylonitic fabrics overprinted by brittle faults developed in a transpressional regime near Paposo at c. 25°S (Ruthven et al. 2020). The variation in geometry and deformation style is likely due to the NNW to NNE variation in fault orientation relative to the SE-directed Cretaceous subduction direction (Ruthven et al. 2020). Overall, the fault system is highly segmented, with the Salar del Carmen, Paposo and El Salado segments each comprised of several parallel or subsidiary branches rather than a single regional-scale fault (e.g. Godoy and Lara 1998; Lara and Godoy 1998; Escribano et al. 2013; Espinoza et al. 2014; Álvarez et al. 2016). Of the three major segments, we focused on the northern El Salado segment to take advantage of the excellent exposure of pre-, syn- and post-kinematic igneous units available for constraining the slip history of the AFS.

The El Salado segment

The El Salado segment represents half of the total AFS length, extending c. 490 km along the Coastal Cordillera between Taltal

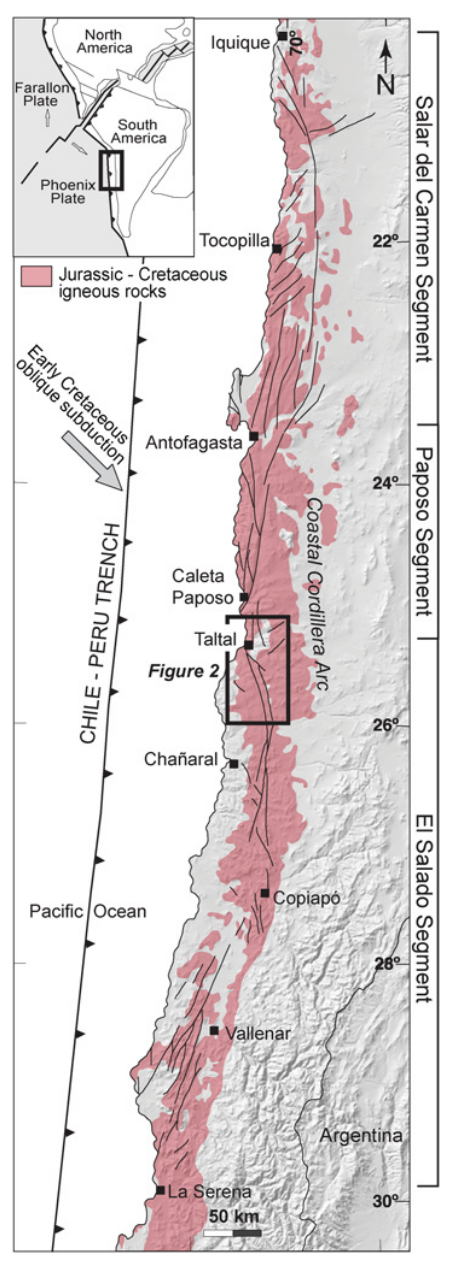


Fig. 1. Regional scale geometry of the oblique subduction system in northern Chile modified from Cembrano *et al.* (2005). Distribution of Jurassic–Cretaceous igneous rocks of the Coastal Cordillera arc are shown in red. The three segments of the Atacama fault system (AFS) are overlain on present-day topography. The northern Salar del Carmen segment stretches from Iquique to Antofagasta, the central Paposo segment stretches from Antofagasta to Caleta Paposo, and the southern El Salado segment stretches from Taltal to La Serena. This study focuses on the northern El Salado segment (study area of Fig. 2 shown in the bold black box). The grey arrow shows the Mesozoic convergence vector from Jaillard *et al.* (1990). The inset map shows approximate plate configuration coeval with Mesozoic sinistral strike-slip deformation along the AFS from Jaillard *et al.* (1990).

(25.4°S) and La Serena (30°S) (Fig. 1). This study focused on the northern half of the El Salado segment between 25.36°S and 26.00°S (Figs 1 and 2), a well-defined segment where kilometrescale zones of steeply dipping, sinistral mylonitic fabrics are exposed and overprinted by brittle structures (e.g. Seymour *et al.* 2020). Rocks exposed along the El Salado segment are predominantly plutons ranging in age from 210 Ma to 107 Ma,

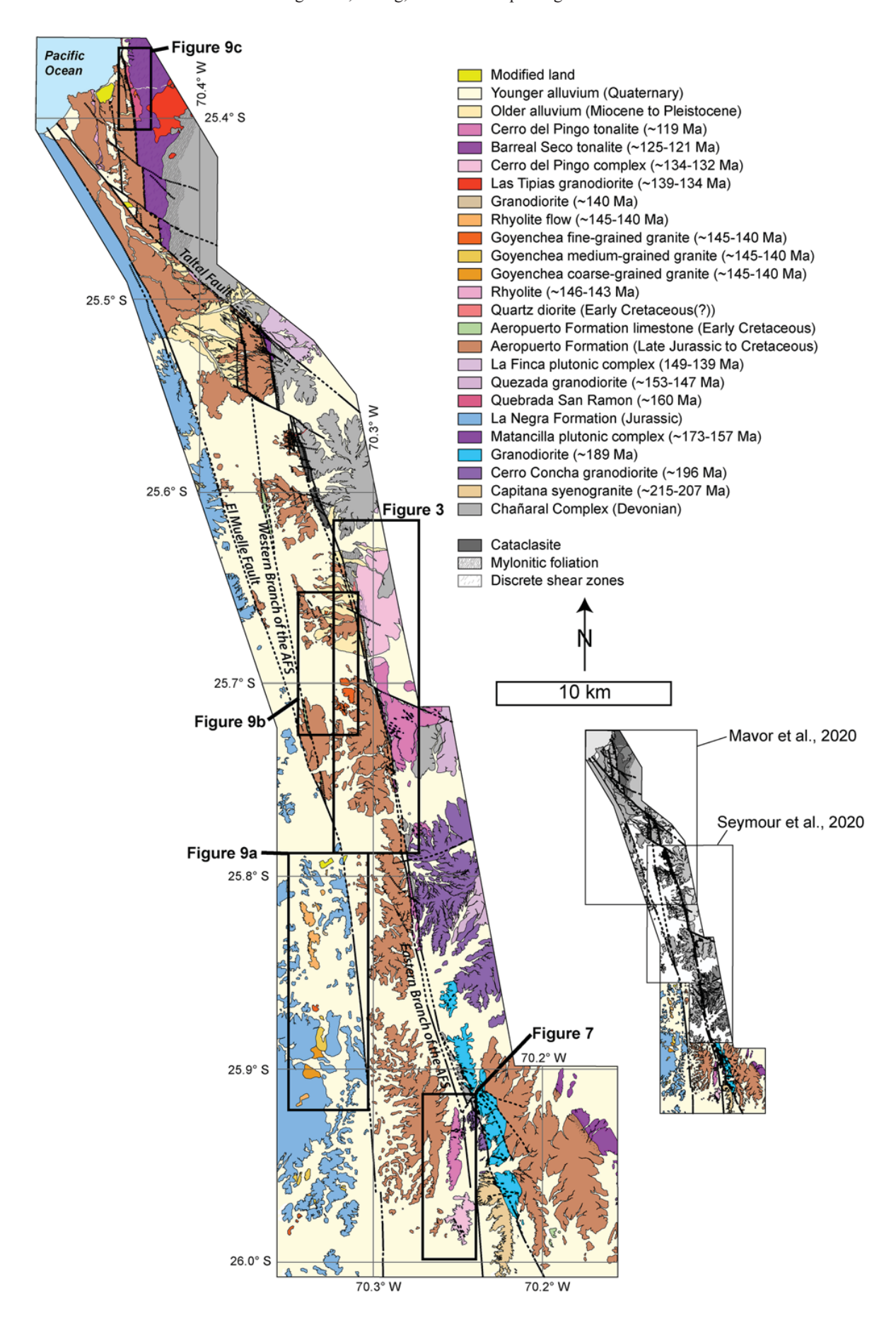


Fig. 2. Simplified map of the northern El Salado segment study area compiled from our new mapping and published work by Escribano *et al.* (2013), Espinoza *et al.* (2014), Seymour *et al.* (2020) and Mavor *et al.* (2020). The Cerro del Pingo Complex is shown in pink, the Jurassic plutons are shown in purple and blue, and the Chañaral Complex is shown in grey. Bold black lines show the major strands of the AFS and mylonites are shown by the wavy pattern. Black boxes show the locations of the inset maps in Figures 3, 7 and 9.

Jurassic to Early Cretaceous volcanic and volcaniclastics (La Negra and Aeropuerto Formations), and lesser volumes of Paleozoic phyllites and quartzites (Godoy and Lara 1998, 1999; Lara and Godoy 1998; Godoy et al. 2003; Arévalo 2005; Contreras et al. 2013; Escribano et al. 2013; Espinoza et al. 2014; Álvarez et al. 2016). Deformation along the El Salado segment is tied to activity of the Coastal Cordilleran arc between 140 and 110 Ma, with Early Cretaceous plutons spatially and temporally associated with AFS deformation. Elevated geothermal gradients thermally weakened the crust and enabled ductile strain at shallow crustal levels, facilitating mylonitization along the margins of Early Cretaceous plutons and surrounding metasedimentary rock. Ductile deformation transitioned to brittle deformation with waning arc magmatism, and the cessation of slip occurred as the arc cooled and migrated eastward at c. 116-99 Ma (Seymour et al. 2020).

The brittle AFS is composed of two well-defined, well-exposed branches that are regionally continuous for at least 130-180 km (Lara and Godoy 1998; Godoy and Lara 1999; Escribano et al. 2013; Espinoza et al. 2014), referred to as the eastern and western branches (Figs 1 and 2). The eastern branch is mapped for c. 180 km along a c. 350° trend as a discontinuous trace of two main strands each with several subsidiary faults, locally represented by metre- to decametre-scale chlorite- and epidote-rich cataclasite fault cores. The eastern branch appears to be the major strand based on its continuity to the south, and primarily separates Jurassic and Early Cretaceous plutons of the Coastal Cordilleran arc and Paleozoic metasedimentary rocks of the Devonian-Carboniferous Chañaral Complex on the east side from Lower Jurassic to Lower Cretaceous volcanic and volcaniclastic deposits on the west side (Lara and Godoy 1998; Godoy and Lara 1999; Escribano et al. 2013; Espinoza et al. 2014). The western branch is mapped for c. 130 km along a c. 350-355° trend on 1:100 000-scale geologic maps and primarily separates Jurassic La Negra Formation volcanic and intercalated marine deposits on the west from Lower Cretaceous Aeropuerto Formation volcanic and volcaniclastic deposits on the east. The El Muelle fault splays off the western branch at 25.78°S and curves from a 340-345° trend at the point of divergence to a 325-330° trend as it enters the Pacific Ocean at 25.41°S (Fig. 2).

The AFS has been recognized as a regional-scale structure since at least 1960 (St. Amand and Allen 1960), yet no clear geologic offset has been identified. Estimates of sinistral displacement magnitude along this segment range from c. 70 km to <20 km. Brown et al. (1993) proposed c. 70 km of brittle sinistral displacement along the AFS by correlating broad zones of ductile deformation north of Taltal with ductile shear zones located to the south. This interpretation relies on the original continuity of the Paposo and El Salado segments, which are separated by a c. 28 km offshore gap where the AFS may be linked, and does not provide an estimate of slip during ductile deformation. More recent studies by Grocott and Taylor (2002) and Seymour et al. (2020) identified AFS mylonite zones in between these segments, casting doubt on the Brown et al. (1993) mylonite zone offset markers. Grocott and Taylor (2002) argued that the displacement is unlikely to exceed 20 km total with no more than a few kilometres across any individual strand due to the discontinuous, overstepping nature of AFS fault branches. Hervé (1987b) documents c. 34 km of Early Cretaceous sinistral slip along the subsidiary Izcuña branch of the Paposo segment based on the offset and correlation of a c. 144 Ma granodiorite body; however, no similar offset markers have been

documented along the El Salado segment even though the entire segment has been mapped at 1:100 000 scale (Arévalo 1995, 2005; Godoy and Lara 1998; Lara and Godoy 1998; Blanco *et al.* 2003; Godoy *et al.* 2003; Welkner *et al.* 2006; Arévalo and Welkner 2008; Arévalo *et al.* 2009; Creixell *et al.* 2012; Contreras *et al.* 2013; Escribano *et al.* 2013; Espinoza *et al.* 2014; Álvarez *et al.* 2016).

Near Taltal, c. 110-107 Ma unstrained dikes cut AFS-related cataclasite and are in turn cut by several branches of the Taltal fault system (TFS), recording the transition between sinistral slip along the north-south-striking AFS and NW-striking TFS (Mavor et al. 2020; Seymour et al. 2020). The TFS offsets the main AFS strands by a total of c. 11 km (Arabasz 1968; Naranjo and Puig 1984; Espinoza et al. 2014; Mavor et al. 2020). The end of strike-slip motion along the AFS is most likely related to changing plate motion that resulted in a transition to approximate east-west crustal shortening across the Taltal and Chivato fault systems and migration of arc magmatism inboard (e.g. Scheuber et al. 1994; Haschke et al. 2006; Ramos and Folguera 2009), broadly coeval with the westward advance of the South American plate and onset of seafloor spreading in the South Atlantic (e.g. Matthews et al. 2012; Seton et al. 2012; Maloney et al. 2013; Granot and Dyment 2015; Kirsch et al. 2016). Neogene east-side-down motion has been documented along the AFS (Hervé 1987a; González and Carrizo 2003; González et al. 2006; Allmendinger and González 2010); however, this motion is absent or limited to metre-to-decimetre scale dip-slip along parts of the northern El Salado segment (Arabasz 1971) and does not obscure structures related to Cretaceous sinistral slip.

Methods

Field mapping, petrography and kinematic analysis

We integrated and expanded upon the study areas of Seymour et al. (2020) and Mayor et al. (2020) to include a 70 km long, 5 km wide swath across the El Salado segment from the Pacific Ocean at 25.36°S to 26.00°S (Fig. 2) to identify potential offset markers across the AFS. Detailed 1:25 000-scale geologic mapping was undertaken to understand the distribution of ductile and brittle structures related to the AFS. We documented lithologies as well as the geometry and kinematics of mylonitic fabrics and brittle faults. The freshest possible samples of plutons deemed potential offset markers in the field were collected for petrography, geochemistry and geochronology (Table 1, Table 2). Hydrothermal alteration, where present in petrographic samples, does not fully replace primary igneous phases, and we report quartz-alkali feldspar-plagioclase modal percentages based on the primary mineralogy (Supplementary File 1). Offset features, R- and T-fractures, and mineral growth steps were used to determine slip sense (e.g. Petit 1987).

Faults were classified based first on their association with either the western or eastern branch of the El Salado segment, then their proximity to the mapped trace of the fault (Supplementary File 2). Faults listed as 'Western Branch' or 'Eastern Branch' include principal slip planes and parallel faults that occur within 50 m of the mapped trace of the major AFS branches; faults labeled 'AFS Parallel' occur >50 m away from but strike ≤30° of the average orientation of the principal slip plane structures. Structural data were analyzed using Stereonet (Allmendinger *et al.* 2011; Cardozo and Allmendinger 2013) and FaultKin (Allmendinger *et al.* 2011). Maximum eigenvectors were used to determine average orientations,

Table 1. Summary of U-Pb sample lithology, degree of strain, and geo/thermochronometric data

	UTM C	UTM Coordinates*					U-Pb				(C)	(U-Th)/He	
Sample	Easting (m)	Northing (m)	Easting (m) Northing (m) Lithology Unit Name	Unit Name	Deformation	Range of Dates (Ma)	Age (Ma)	Age (Ma) 2σ n†	MSWD	ge	o n†	1σ n† SE Alt SE 2 Max SE‡	2 Max SE‡
161-74 - cores	374811	7131132	Bt-Hbl Tonalite	Bt-Hhl Tonalite Cerro del Pingo Complex Protomylonitic	Protomylonitic	- 141.4	131.9	131.9 1.3 51			8.2 5/6	5/6 3.7 2.8	7.3
161-74 - rims	374811	7131132	Bt-Hbl Tonalite	Bt-Hbl Tonalite Cerro del Pingo Complex Protomylonitic	Protomylonitic	114.9 - 121.7	119.5	119.5 1.8 10	2.4			5/6 3.7 2.8	7.3
181-N154	375288	7125806	Hbl Tonalite	Hbl Tonalite Cerro del Pingo Complex Protomylonitic/Discrete	Protomylonitic/Discrete	125.6 - 140.7	134.0	0.8 62/69 6.5		99.1	.1 3/4	3/4 0.6 2.8	5.6
					Zones								
188-S142	366809	7161211	Granite	Leucocratic Plutons	Unstrained	133.2 - 151.1	140.9	1.1 52/67 8.6	9.8		1		
191-N46	366334	7138243	Granite	Leucocratic Plutons	Unstrained	135.9 - 153.1	143.0	1.8 27/40	7.7		•	1	
201-SM482	355119	7191625	Granite	Leucocratic Plutons	Unstrained	131.7 - 134.7,	160.6	0.8 36/49	3.6	1	•	1	
						155.0 - 169.1							
201-SM458 - rims 355383	s 355383	7191168	Granite	Leucocratic Plutons	Unstrained	143.7 - 174.1	163.8	0.8 49	3.9		1	1	
201-SM458 - rims 355383	s 355383	7191168	Granite	Leucocratic Plutons	Unstrained	137.2 - 175.9	160.1	3.2 10	5.0		ı	1	

*Coordinates in Universal Transverse Mercator (UTM) World Geodetic System 1984 (WGS84) in denotes number of grains used to calculate mean age

'Age provided by youngest 3 grains 'Age perovided by youngest 3 grains tage determined from lower Terra-Wasserburg Intercept ‡SE denotes Standard Error Standard error = $\ln \sqrt{\operatorname{std}} \operatorname{dev}$ Alternative Standard error = $\frac{1}{N} \sqrt{\sum_i \sigma_{si}^2}$ where σ_{xi} is the single grain error

Table 2. Whole-rock geochemical data

	161-62	161-74
Major and Minor E	lements (%)	
SiO2	63.80	62.10
Al_2O_3	16.45	16.55
Fe_2O_3	5.47	5.62
CaO	5.15	5.56
MgO	2.47	2.51
Na ₂ O	3.81	4.60
K_2O	2.16	1.12
Cr_2O_3	< 0.01	< 0.01
TiO ₂	0.63	0.63
MnO	0.12	0.07
P_2O_5	0.10	0.19
SrO	0.04	0.05
BaO	0.04	0.03
LOI	0.70	1.16
Total	100.94	100.19
Trace elements (ppi		
Ba	398.00	298.00
Ce	35.70	39.20
Cr	10.00	20.00
Cs	2.44	1.37
Dy	3.94	3.08
Er	2.28	1.89
Eu	1.04	1.35
Ga	19.10	19.30
Gd	3.86	3.37
Hf	3.60	4.70
Но	0.80	0.64
La	17.00	18.80
Lu	0.36	0.27
Nb	4.40	5.50
Nd Pr	18.50	19.90
	4.55	4.97
Rb Sm	59.90 4.50	40.50 4.18
Sn	2.00	
Sr	401.00	3.00 490.00
Ta	1.40	2.20
Tb	0.63	0.51
Th	5.46	3.67
Tm	0.37	0.27
U	1.33	0.27
V	141.00	114.00
W W	207.00	332.00
W Y	22.00	17.30
Yb	2.36	1.82
Zr	126.00	191.00
LI	120.00	191.00

and incremental shortening and extension (P- and T-) axes were determined from paired fault plane and slickenline lineation measurements (Marrett and Allmendinger 1990). We present fault plane solutions derived from linked Bingham P- and T-axes of faults with field-determined slip sense as well as modeled results assuming a sinistral slip sense on all approximate north-south-striking slickensided faults with unclear kinematics. Given the consistent sinistral kinematics along the AFS, these modeled results are likely to be largely accurate and allow us to evaluate kinematic patterns that are not influenced by incomplete slip sense determination.

Analytical methods

For U-Pb analysis, zircon grains separated from samples 161-74, 181-N154, 191-N46, 188-S142, and 201-SM458 were mounted in

epoxy, polished to expose the center of the grains, and imaged using cathodoluminescence (CL) to document internal zoning patterns. Laser ablation inductively coupled plasma mass spectrometry spot analyses targeted individual growth domains determined from CL imagery. Additional euhedral, unpolished zircon grains from samples 161-74, 181-N154, and 201-SM482 were mounted on double-sided tape parallel to the c-axis and depth profiled according to the methods outlined in Marsh and Stockli (2015) and detailed in Seymour et al. (2020) to resolve fine-scale growth domains too small for a spot analysis. All U-Pb analyses were conducted at the University of Texas at Austin in the UTChron facilities. The combined internal and external error is reported for individual grains (Supplementary File 3). Grains were filtered to ${<}10\%$ discordance to eliminate the effects of disturbance due to Pb loss and/or inheritance. Weighted ²⁰⁶Pb/²³⁸U average dates with 2σ error calculated in Isoplot 4.15 (Ludwig 2003) are reported (Table 1).

(U-Th)/He analyses were conducted on samples 161-74 and 181-N154 at the University of Texas at Austin according to the methods outlined in Wolfe and Stockli (2010). Aliquots were assigned an 8% analytical error based on the long-term laboratory reproducibility of the Fish Canyon Tuff zircon standard (e.g. Reiners *et al.* 2002, 2004). Four to seven grains were analyzed per sample. Dates are reported based on the average of 3–6 single grains per sample (Supplementary File 4). Error is reported as twice the larger of either the traditional or alternative standard error of the average calculation (Table 1). Whole-rock sample volumes of relevant plutons were analyzed for major and minor element composition by inductively coupled plasma atomic emission spectroscopy at ALS Minerals in Reno, Nevada (Table 2).

Results

We documented the occurrence of spatially restricted mylonitic shear zones in two distinct areas on opposite sides of the eastern branch, each associated with a suite of pre- and synkinematic intrusions that bear striking petrographic resemblances to one another (Fig. 2). Here we suggest the association of metasedimentary mylonites developed in the thermal aureole of a set of petrographically, geochemically and geochronologically identical intrusions together constitute an offset marker along the El Salado segment because the mylonite zones and associated intrusions together can be tied to a single thermal aureole in a unique location along the El Salado segment. We further note the similarity of two belts of leucocratic igneous bodies across the western branch (Fig. 2). We present a description of the petrography and textures of each set of potentially correlative igneous bodies and compare new zircon U-Pb crystallization dates, (U-Th)/He cooling dates (Table 1) and whole-rock geochemistry (Table 2) to data presented in Seymour et al. (2020) to establish a robust offset marker for the El Salado segment of the AFS.

Eastern branch

Mylonite zone east of the eastern branch of the AFS (25.61°S and 25.78°S)

A c. 18 km long mylonite zone occurs between 25.61°S and 25.78°S where the Cerro del Pingo Plutonic Complex is adjacent to the eastern branch and extends along-strike into the neighboring Chañaral Complex (Fig. 3). The Cerro del Pingo Complex in this zone is a fresh, medium-grained mesocratic hornblende biotite granodiorite to biotite hornblende tonalite locally crosscut by adularia + quartz veinlets (samples 181-S55 and 188-S156 in Figs 4 and 5). Seymour et al. (2020) presents 132.6 \pm 0.9 Ma and 132.3 \pm 1.3 Ma zircon U–Pb dates for this body. Protomylonitic fabrics within the tonalite are locally developed in the central c. 14 km long portion of the shear zone that ranges from c. 200–800 m

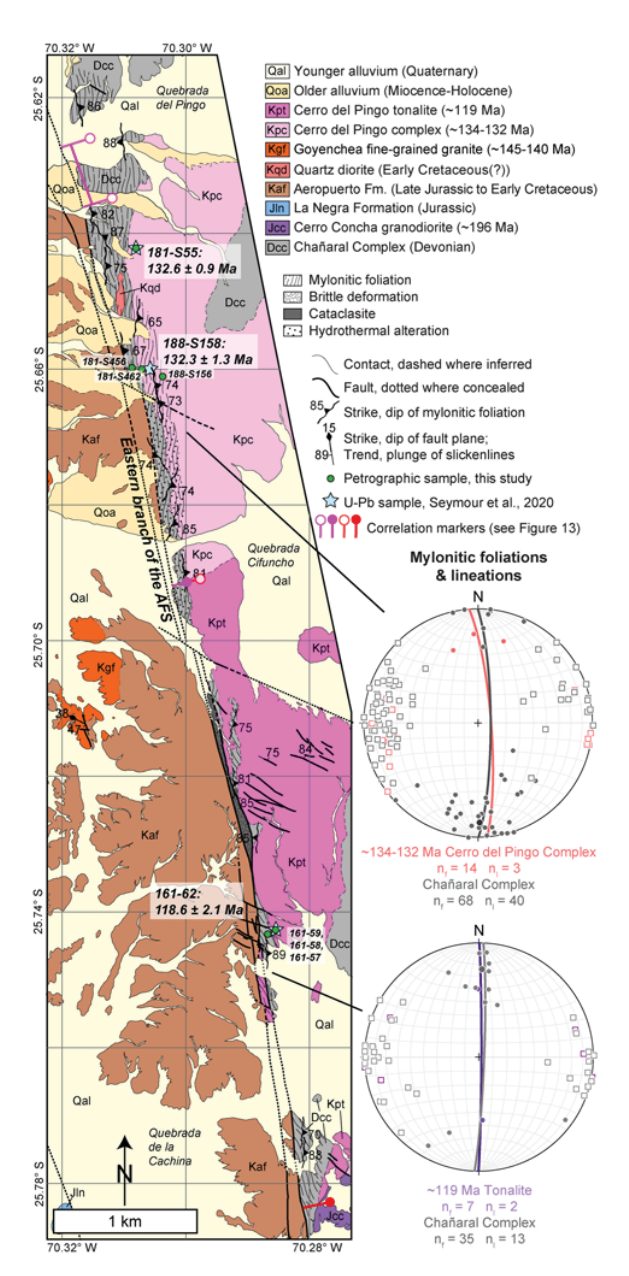


Fig. 3. Inset map of the northern mylonite zone and Cerro del Pingo Complex east of the eastern branch of the AFS. Blue stars show U–Pb dates from Seymour *et al.* (2020). Equal-area stereograms of mylonitic foliations from the *c.* 132 Ma Cerro del Pingo Complex (top. pink), *c.* 119–120 Ma tonalites (bottom, purple) and adjacent metasedimentary mylonites for each pluton (both plots, grey) are shown. Individual measurements are shown as poles to planes with empty squares (foliations) and dots (lineations). Average orientations are given by bold great circles and bold dots.

wide where the Cerro del Pingo Complex intrudes Chañaral Complex metasedimentary rocks, extending up to c. 300–400 m into the pluton itself. Metasedimentary rocks are pervasively highly strained. In the central part of the shear zone both quartz-rich and phyllosilicate-rich lithologies are entirely dynamically recrystallized with mylonitic foliation planes defined by micas and lineations defined by stretched quartz. Within the Cerro del Pingo Complex, protomylonitic fabrics are defined by recrystallized tails on feldspar porphyroclasts, fine-grained mixtures of altered feldspar and sericite, aligned chloritized biotite and hornblende, and lenses of recrystallized quartz (samples 188-S156 and 181-S456 in Fig. 4).

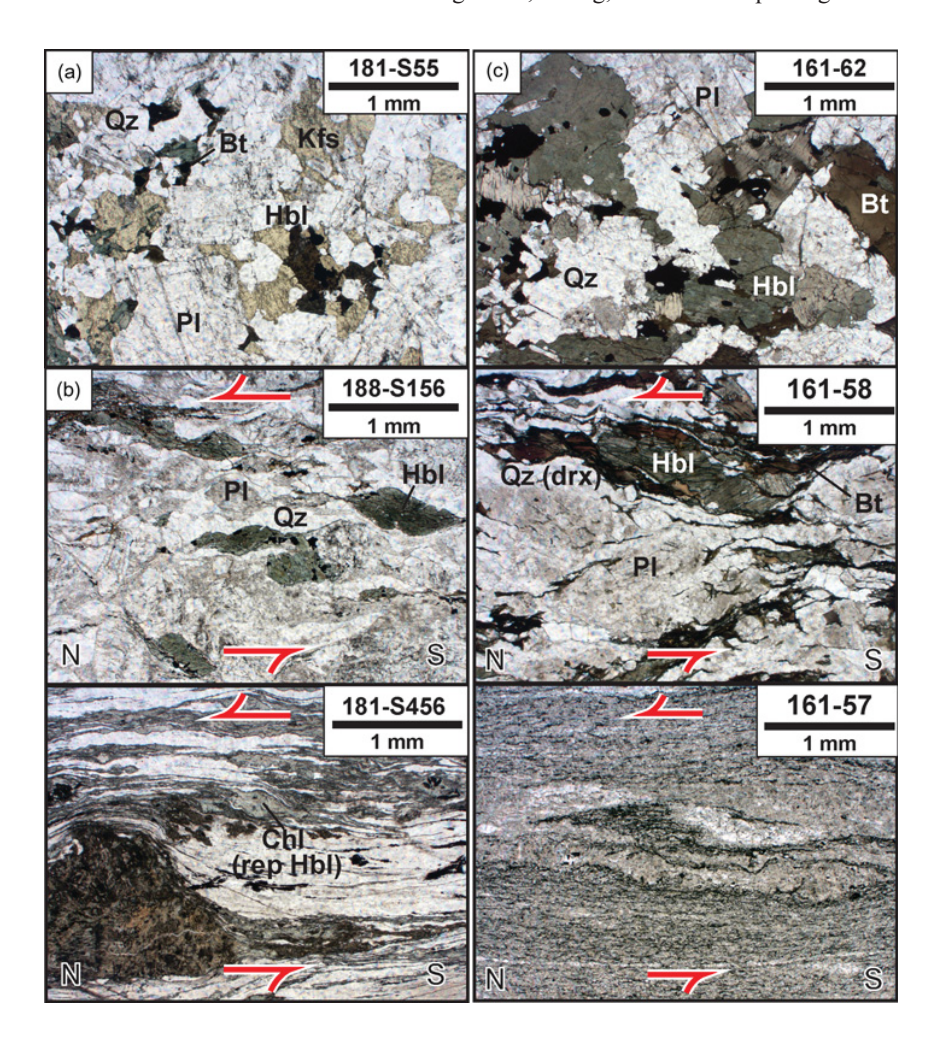


Fig. 4. Photomicrographs in planepolarized light corresponding to different degrees of mylonitic deformation at locations specified in Figure 3. Samples are spatially related with the U-Pb sample locations from Seymour et al. (2020): the sample most distal to the AFS is at the top and proximity to the AFS increases towards the bottom. (a) Older nonmylonitic Cerro del Pingo Complex U-Pb sample 181-S55, (b) older mylonitic Cerro del Pingo Complex sample 188-S156 (adjacent to U-Pb sample 188-S158) and mylonitic Chañaral Complex sample 181-S456, and (c) younger Cerro del Pingo Tonalite U-Pb sample 161-62 and mylonitic to ultramylonitic samples (161-58 and 161-57, respectively). Sample 161-57 is derived from the Chañaral Complex. Abbreviations are as follows: Bt = biotite; Chl = chlorite; Hbl hornblende; Kfs = potassium feldspar; Qz = quartz; Pl = plagioclase; Ser = sericite; drx = dynamically recrystallized; rep = replaced. Samples with fabrics were cut perpendicular to foliation and parallel to lineation. Orientations and shear sense (red arrows) are noted where present.

The degree of strain increases with proximity to the eastern branch, and some samples are mylonitic rather than protomylonitic (e.g. sample 181-S456 in Fig. 4). The average orientation of the mylonitic foliation is 356/81 E (right-hand-rule strike/dip) within the pluton and 000/81 E within the quartzite mylonites (Fig. 3, Supplementary File 2). The quartzite mylonites have a dominantly south-plunging lineation (average lineation 179/15). A strain gradient within the metasedimentary rocks where quartzites grade from platy mylonites to statically recrystallized but unstrained records the northern limit of mylonitization where the AFS juxtaposes the Chañaral Complex against the Aeropuerto Formation (Seymour *et al.* 2020). The brittle core of the eastern branch cuts mylonitic and protomylonitic fabrics, and is oriented *c.* 14° counterclockwise of the average mylonitic foliation, consistent with sinistral shear.

Between 25.70°S and 25.78°S, the c. 133–132 Ma Cerro del Pingo Complex is intruded by a mesocratic tonalite (Fig. 3). Near this contact, the Cerro del Pingo Complex is highly altered with silicification and adularia veining. The younger intrusive rock is fresher and distinctly black and white compared to other plutons in the area, which are often present as a medium gray. Mineralogically, the younger phase is a hornblende–biotite tonalite (sample 161-62 in Figs 4 and 5). Dark enclaves of quartz diorite are common. Cathodoluminescence imagery shows individual zircons have cores and rims (Fig. 6). Cores have igneous textures and U–Pb analyses on polished mounts yield a weighted mean date of 128.1 \pm 0.5 Ma (n = 59, MSWD = 1.8; sample 161-62). The rims were too thin to analyze in polished mounts, so additional grains were depth-profiled. Dates younger than the cores were interpreted to

capture rim growth. The weighted mean date of rims (118.6 \pm 2.1 Ma, n = 11, MSWD = 3.5) is interpreted to record crystallization of this younger tonalite. The (U-Th)/He zircon cooling date is $100.2 \pm 12.9 \,\mathrm{Ma}$ with individual aliquots ranging from 119.6 to 85.2 Ma (Seymour et al. 2020). A sinistral shear zone up to c. 220 m wide with a subvertical, NNE-striking foliation (002/86 E) and north-plunging lineation (001/24) is developed in Chañaral Complex metasedimentary rocks and the western margin of this pluton (Fig. 3, Supplementary File 2). The brittle eastern branch is oriented c. 13° counterclockwise of the average mylonitic foliation. Within the tonalite, protomylonitic fabrics are defined by biotite, dynamically recrystallized quartz and fractured feldspar porphyroclasts. The highest degree of strain in the tonalite occurs in sills within the metasedimentary rocks or discrete mylonite zones near the pluton margins (e.g. sample 161-58 in Fig. 4). Strain decreases with increasing distance from the eastern branch, grading from protomylonitic to unstrained with locally developed magmatic fabrics defined by aligned biotite and hornblende c. 50 m into the pluton. The mafic phases and plagioclase within the protomylonitic and unstrained portions of the pluton are fresher than those of the c. 133-132 Ma pluton. Sinistral strain in the quartzites and phyllites is recorded by bulging and subgrain rotation recrystallization of quartz grains, oblique grain shape fabrics and asymmetric intrafolial folds (sample 161-57 in Fig. 4). A strain gradient is developed to the south where the eastern branch juxtaposes the Jurassic Cerro Concha granodiorite against the Aeropuerto Formation, and quartzites grade from platy mylonites to statically recrystallized but unstrained <1 km south of the c. 119 Ma tonalite along the eastern branch.

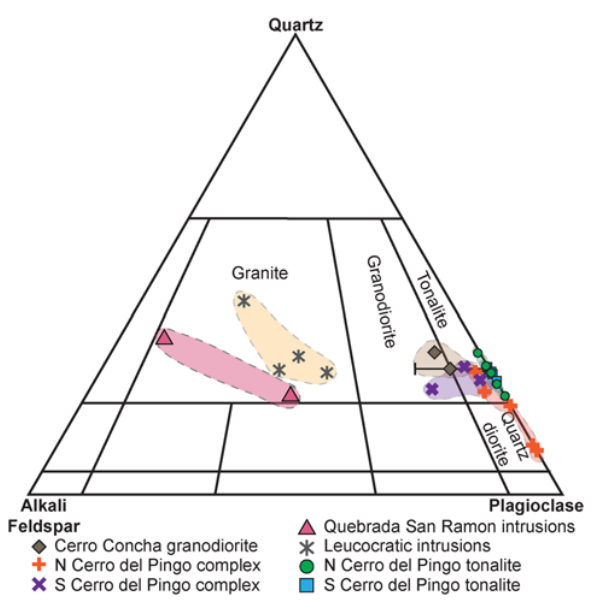


Fig. 5. Ternary diagram showing the compositions of the Cerro Concha granodiorite (brown diamonds), northern c. 133–132 Ma Cerro del Pingo complex (red crosses), southern c. 134 Ma Cerro del Pingo complex (purple crosses), northern c. 120–119 Ma Cerro del Pingo tonalite (green circles), southern c. 120–119 Ma Cerro del Pingo tonalite (blue squares), leucocratic intrusives (grey six-pointed stars), and Quebrada San Ramon intrusions (purple triangles). Compositions were determined by counting 100 random points per thin section and mineral abundances record primary igneous mineralogy. The error bar on the Cerro Concha sample indicates uncertainty in determining plagioclase from potassium feldspar due to extensive sample alteration.

Mylonite zone west of the eastern branch of the AFS (25.92°S and 25.99°S)

Another mylonite zone within metasedimentary rocks and synkinematic tonalitic plutons is located c. 21 km south of the previously described mylonite zone, exposed for c. 6.3 km along strike of the western margin of the c. 175–177°-trending eastern branch between 25.92°S and 25.99°S (Figs 2 and 7). The pluton exposed at the northern end of this mylonite zone is a fresh hornblende biotite tonalite (sample 161-74 in Figs 5 and 8b). As with the mesocratic tonalite to the north on the eastern side of the fault (Fig. 4), the rock is distinctly black and white and crosscut by sub-parallel adularia + quartz veinlets. Similar to the northern mylonite zone, the shear zone is c. 200 m wide and extends up to c. 120 m into a mesocratic pluton that intrudes the metasedimentary mylonites along the western margin. Aligned hornblende and biotite and recrystallized tails of feldspar define protomylonitic fabrics within the pluton (average foliation orientation 015/85 E) (Fig. 7, sample 161-74b in Fig. 8b, Supplementary File 2). Silicification of the tonalite and the metasedimentary mylonites occurs within 400 m of the eastern branch and intensifies with proximity to the Cathodoluminescence imagery of zircons shows igneous textures as well as cores and rims (Fig. 6). The weighted mean date of the cores derived from spot analyses is $131.9 \pm 1.8 \text{ Ma}$ (n = 51, MSWD =6.7, sample 161-74; Fig. 6) and the weighted mean date of rims derived from depth profiles is $119.5 \pm 1.8 \text{ Ma}$ (n = 10, MSWD = 1.8 Ma) 2.4). The average (U-Th)/He zircon cooling date is 99.0 \pm 7.3 Ma and individual aliquots range from 107.2 to 86.8 Ma (Table 1, Supplementary File 4). Metasedimentary rocks at this location are more arkosic than the northern region, and fine-grained recrystallized feldspar defines foliations in addition to recrystallized quartz. Subvertical mylonitic fabrics strike north-south (000/81 E), and lineations rake shallowly (177/14) from the south (Fig. 7). The brittle eastern branch is oriented *c.* 10° counterclockwise of the average mylonitic foliation, consistent with sinistral shear, and clasts of mylonitic quartzite are abundant within the cataclastic damage zone of the AFS.

Exposure of the metasedimentary mylonite screen and the eastern branch of the AFS is covered by alluvium to the south, and the shear zone narrows to c. 15 m with variable degrees of protomylonitic fabric development with more localized centimetre- to metre-scale shear zones as the lithology transitions from an older mesocratic hornblende tonalite-quartz diorite (samples 171-N338 and 181-N154 in Figs 5 and 8). The pluton, which is intruded by the c. 120-119 Ma tonalite described above, is crosscut by adularia + quartz veinlets with selvages defined by potassium alteration of surrounding phases. Hornblende is often chloritized, and individual portions of the pluton have up to 6–19% secondary chlorite. Discrete zones of steep north- to NE-striking mylonitic foliation are concentrated along the eastern exposures of the pluton (Fig. 7, Supplementary File 2). We note that the eastern branch is located up 300 m away from most of this exposure under alluvial cover, and most of the exposure of the pluton retains unstrained magmatic textures with no mineral alignment. This pluton has a zircon U–Pb date of 134.0 \pm 0.8 Ma (sample 181-N154, n = 62/69; MSWD = 6.5, Fig. 6) and a zircon (U-Th)/He (ZHe) date of 99.1 \pm 1.2 Ma with a tight cluster of individual grain dates at 99.7–97.8 Ma (Table 1).

Non-mylonitized lithologies across the eastern branch Our 1:25 000-scale mapping indicates that there are no other occurrences of significant AFS-related mylonite zones along the c. 70 km length of the El Salado presented here. Pre-kinematic Jurassic plutons along the eastern branch include the c. 196 Ma Cerro Concha granodiorite and a c. 189 Ma Jurassic granodiorite (Fig. 2, Seymour et al. 2020). The Cerro Concha granodiorite occurs on both sides of a major NW-trending splay off the eastern branch, sinistrally separated by c. 11–15 km. On the western side of the NW-striking fault, the Cerro Concha pluton is leucocratic due to extensive alteration. The along-strike strain gradient from highstrain mylonites in and adjacent to the Early Cretaceous Cerro del Pingo Complex to brittle fracturing and faulting in the Early Jurassic Cerro Concha granodiorite and adjacent Chañaral Complex metasedimentary rocks at the same structural level indicates the Cerro Concha intruded before the onset of AFS-related strain (zircon U-Pb: 195.6 \pm 1.0 Ma and 196.4 \pm 2.2 Ma; Seymour *et al.* 2020) and was relatively cold compared to Early Cretaceous plutons during AFS deformation.

Mylonites are not developed in the Jurassic La Negra Formation volcanics, Cretaceous Aeropuerto Formation volcanics and volcaniclastics, or in the Devonian Chañaral Complex where the metasedimentary rocks are distal to synkinematic plutons. In between the two mylonite zones described above, metasedimentary rocks occur in two narrow slivers bound by fault strands at 25.82°S-25.83°S and 25.89°S-25.92°S (Fig. 2). The northern sliver is 130-170 m wide and contains mylonitic metasedimentary rocks with steep north-south-striking foliation in contact with an altered granodiorite, interpreted here as an altered exposure of the Cerro del Pingo Complex based on its association with metasedimentary mylonites. The northern sliver is bound to the west by cataclastic Aeropuerto Formation volcanics and to the east by highly fractured but internally unstrained metasedimentary rocks and a highly altered granitoid, most likely the southern extent of the Cerro Concha granodiorite. The southern sliver is up to c. 300 m wide and bound by the main eastern branch of the AFS to the west and subsidiary NW-trending fault splays and c. 189 Ma Jurassic granodiorite to the east. The metasedimentary rocks in this sliver are entirely unstrained and either retain original detrital textures or

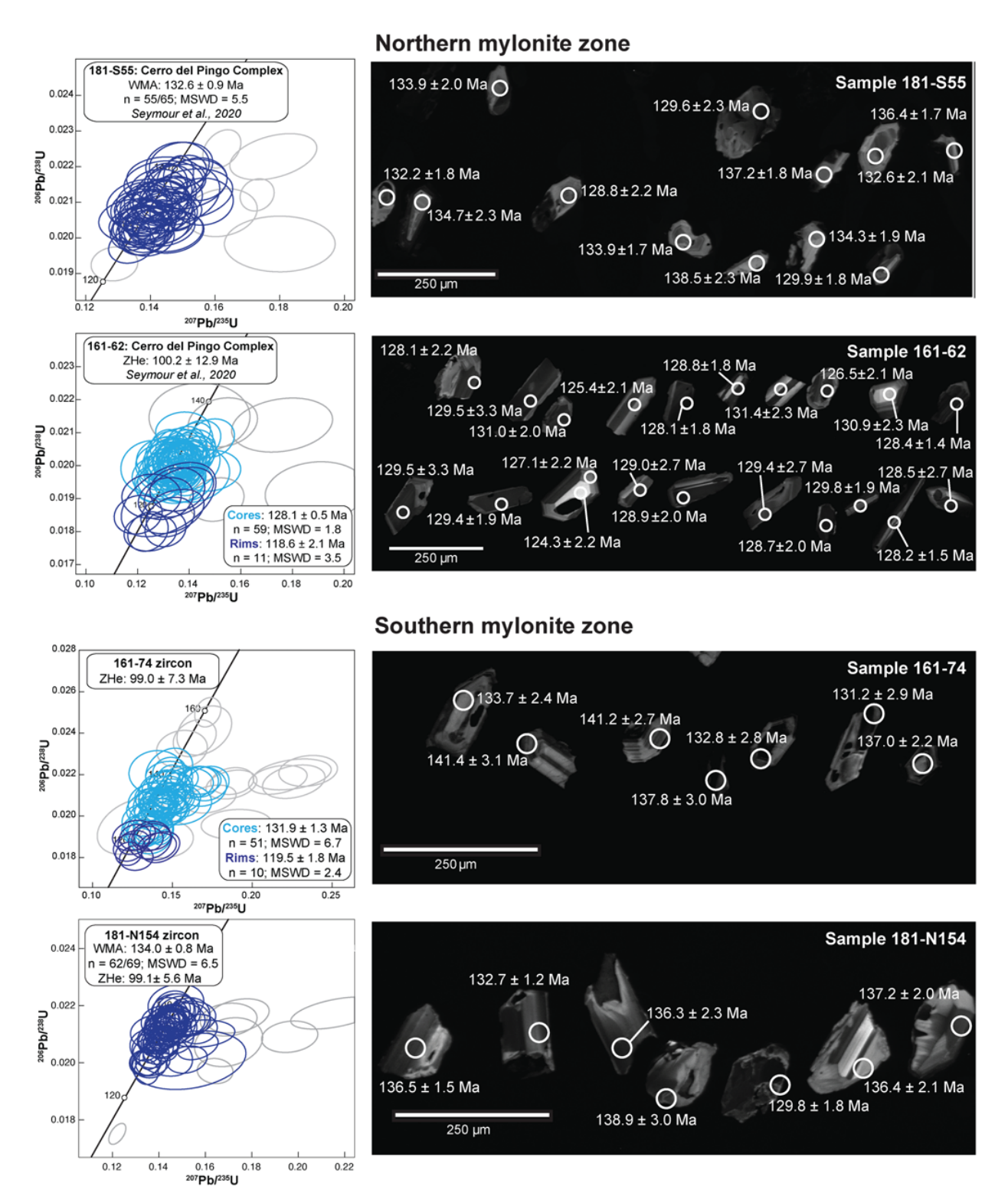


Fig. 6. U–Pb concordia diagrams and representative cathodoluminescence imagery for plutons associated with the northern mylonite zone (top, from Seymour *et al.* 2020) and the southern mylonite zone (bottom). Data have been filtered to 10% discordance and grains with >10% discordance are shown in grey. Uncertainties are reported at 2σ .

are statically recrystallized. Additional reconnaissance work between the southern map boundary and 26.30°S (*c.* 33 km south of the map area) did not identify mylonites along the eastern branch, and mylonites are not represented in this area at the 1: 100 000 scale (Godoy and Lara 1998; Espinoza *et al.* 2014).

Finally, we note that an Early Cretaceous Las Tipias pluton located c. 300-600 m east of the AFS between 25.3 and 25.4°S

does not have an associated mylonite zone, despite its overlap in timing of emplacement with the mylonitic Cerro del Pingo Plutonic Complex. Therefore, we suggest the two occurrences of mylonite zones in synkinematic plutons and adjacent metasedimentary rocks at 25.61–25.78°S and 25.92–25.98°S are unique and can be used an offset marker along the eastern branch of the El Salado segment.

Western branch

Leucocratic bodies with pervasive orange oxidation intrude the La Negra Formation in a NE-SW sub-linear belt west of the western branch of the AFS between 25.79°S and 25.95°S (Fig. 9; Espinoza et al. 2014). These felsic intrusions have textures that range from very fine-grained quartz and feldspar mixtures (<0.2 mm) with phenocrysts of quartz and sanidine at the northern end of the belt to porphyritic intrusive bodies with coarse (2-9 mm) plagioclase and uncommon 2-4 mm clots of epidote, chlorite and oxide phases. interpreted to be replaced mafic phases at the southern end of the belt (Fig. 10a). Several outcrops have interlocking 1-2 mm quartz and potassium feldspar grains between sericitized plagioclase crystals, sometimes with granophyric texture. Rhyolitic flows are also present along this trend (Espinoza et al. 2014). The leucocratic intrusions do not come into direct contact with the AFS and do not record ductile strain. Sample 191-N46 has single grain dates with <10% discordance ranging from 135.9 to 153.1 Ma that give a weighted ²⁰⁶Pb/²³⁸U average date of 143.0 \pm 1.8 Ma (n = 27/40, MSWD = 7.7, Fig. 11) and several older grains ranging from 178.6 to 659.1 Ma.

A similar series of unstrained leucocratic granites with pervasive orange-brown oxidation intrude the Aeropuerto Formation as a NNE-SSW trending chain of low hills west of the eastern branch of the El Salado segment 6-29 km north of the leucocratic intrusions exposed on the western side of the western branch (Fig. 9; Espinoza et al. 2014). Our petrography shows these intrusions are granites with 19-33% 2-3 mm plagioclase, 29-36% 0.5-2 mm potassium feldspar and 30-43% modal quartz, with spherulitic to granophyric intergrowths and spherical bodies of intergrown quartz and epidote (Figs 5 and 10b). Mafic phases are rare and are completely altered to chlorite where present. Potassium feldspar mantling plagioclase and granophyric textures are present. Textures vary moving north to south from very finely intergrown potassium feldspar and quartz that form spherulites to a coarser-grained granophyric intergrowth with defined 0.5-1 mm quartz, plagioclase and potassium feldspar crystals and cavities or spheres filled with quartz and epidote (Fig. 10b). New zircon ²⁰⁶Pb/²³⁸U analyses on one of the felsic plutons between the eastern and western branches of the AFS yield single grain dates with <10% discordance that range from 133.2 to 151.1 Ma with one young (120.5 Ma) and one older (161.7 Ma) grain. The weighted mean of these data is 140.9 ± 1.1 Ma (sample 188-S142, n = 52/67, MSWD = 8.6, Fig. 11).

At the northern end of the El Salado segment at the coastline, a third potentially correlative felsic intrusion is exposed. An unstrained porphyritic granite stock intrudes the Jurassic Matancilla Plutonic Complex east of the eastern branch along Quebrada San Ramon, c. 20-30 km north of the leucocratic intrusions exposed between 25.65°S and 25.71°S (Figs 2 and 9; Espinoza et al. 2014). Our petrographic analysis shows this granite has a matrix of intergrown 1-2 mm potassium feldspar and quartz. The character of the granite is variable within a single outcrop and ranges from mesocratic with c. 30% 2-7 mm moderately sericitized plagioclase, c. 18-20% chloritized hornblende and biotite to a purely leucocratic matrix of potassium feldspar and quartz with c. 7-10% 2-7 mm sericitized plagioclase and <10% altered mafic phases (Figs 5 and 10c). Potassium feldspar occasionally shows perthitic texture and often mantles sericitized plagioclase. Rarely, myrmekitic texture is found in smaller (2-3 mm) plagioclase crystals. Quartz is unstrained. Zircon 206Pb/238U dates from two end-member textural varieties of this intrusion are strongly clustered at c. 163–160 Ma for both core (160.6 \pm 0.8 Ma, sample 201-S482; and 163.8 ± 0.8 Ma, sample 201- SM458) and overgrowth domains (160.1 \pm 3.2 Ma, sample 201-S458; Fig. 11). Several single grain dates with <10% discordance fall outside of this range with three young dates (131.7–134.7 Ma) and three older grains (c. 254, 615 and 1160 Ma).

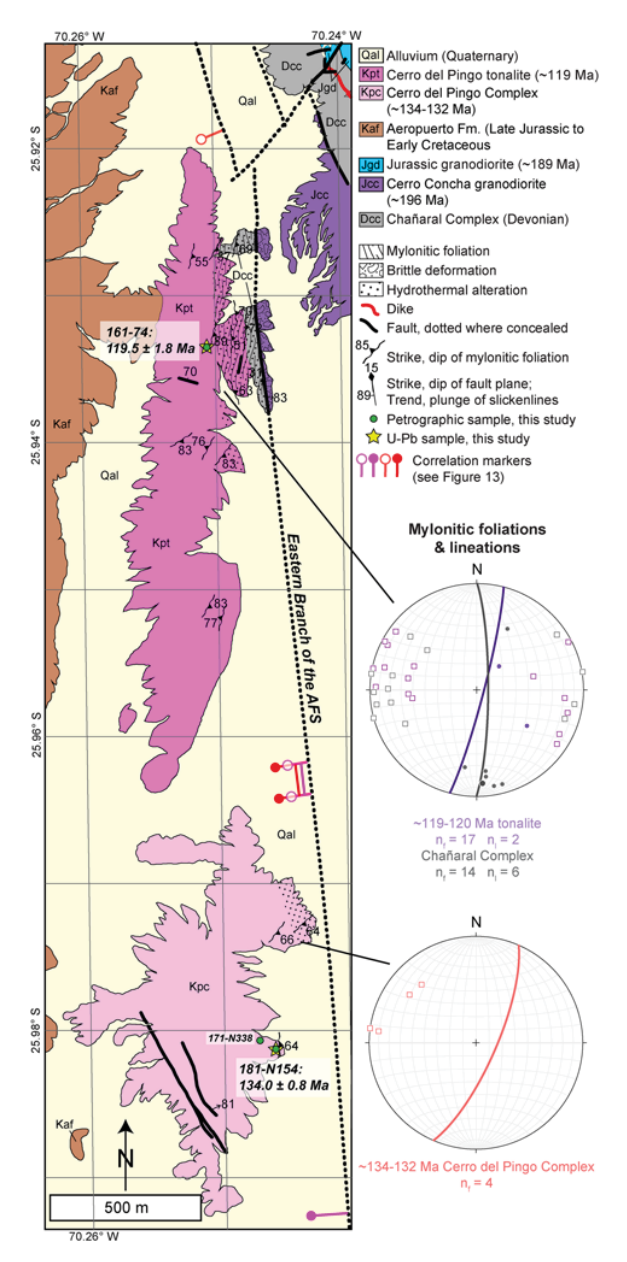


Fig. 7. Inset map of the southern mylonite zone and Cerro del Pingo Complex west of the eastern branch of the AFS. Yellow stars show new U–Pb dates from this study. Stereograms of structural data from the *c*. 134 Ma Cerro del Pingo Complex (bottom, pink), *c*. 120–119 Ma tonalite (top, purple) and adjacent metasedimentary mylonites (gray). Individual measurements are shown as poles to planes with empty squares (faults, foliations) and dots (slickenlines, lineations). Average orientations are given by bold line (foliations) and bold dot (lineations).

Brittle fault kinematics

Brittle fault kinematics derived from the orientation of brittle fault planes, slickenlines, and slip sense indicators are dominantly sinistral strike-slip, with evidence of minor dip-slip motion. Most fault planes strike NNW and are near vertical (Fig. 12, Supplementary File 2). The orientation of faults defining the brittle eastern branch is similar to that of the mylonitic foliations in the northern and southern mylonite zones (Figs 3 and 7, respectively): both are NNW–SSE striking and steeply dipping with shallowly north-plunging slickenlines. The eastern branch has an average slickenline orientation of 354/11 (trend/plunge) on a

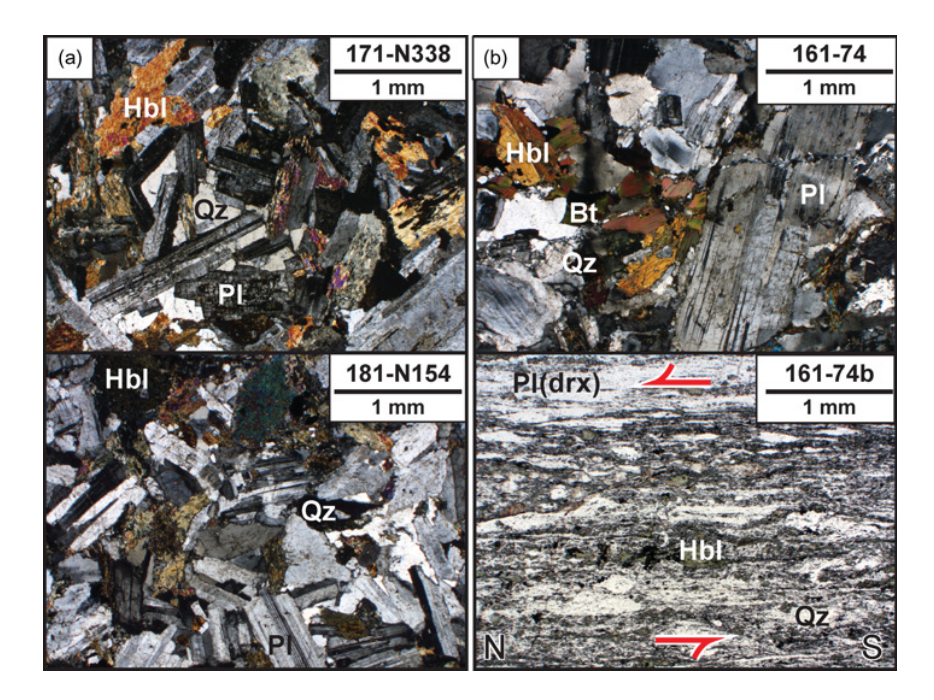


Fig. 8. Photomicrographs in plane-polarized light of the (**a**) *c*. 134 Ma Cerro del Pingo Complex and (**b**) *c*. 120-119 Ma tonalites and associated metasedimentary mylonites of the southern mylonite zone. See Figure 7 for sample locations. Abbreviations are as follows: Bt = biotite; Chl = chlorite; Hbl = hornblende; Qz = quartz; Pl = plagioclase; drx = dynamically recrystallized; rep = replaced.

subvertical north-trending fault (173/89 W; strike/dip, dip direction), and principal slip planes have an average orientation of 352/88 E with slickenlines oriented 357/07 (Supplementary File 2). The average fault gouge foliation is 15° clockwise of the average principal slip plane, consistent with sinistral shear (Fig. 12). These orientations do not vary across the TFS.

Western branch fault planes strike NNW and dip steeply east. The average fault plane orientation in the damage zone is 353/82 E with 345/03 slickenlines, and the principal slip plane orientation is 350/85 E with 354/19 slickenlines. Faults parallel to (strike ≤30° from the average AFS principal slip planes) but not located within the damage zones of either major branch are also northtrending and steeply east-dipping (average plane 357/85 E), with an average slickenline orientation of 171/04 (Fig. 12). The El Muelle fault, which splays off the western branch and most likely continued to slip as a part of the TFS after AFS motion ceased (Mayor et al. 2020), is NW- to NNW-trending and subvertical (average plane 164/90), and is dominated by sinistral strike-slip motion with an average slickenline of 164/00 (Fig. 12). For all fault categories, the data consistently indicate a subhorizontal NW-SE-trending linked Bingham P-axis and subhorizontal NE-SW-trending linked Bingham T-axis (Supplementary File 2). Orientations do not change significantly when only faults with a field-determined sense of slip are included or when sinistral slip on unknown faults is assumed. Together, brittle kinematics record predominantly sinistral strike-slip motion with a minor component of dip-slip motion.

We note that each fault population records 20–28% steep (>45°) dip-slip slickenlines. Map patterns indicate a component of east-side-up motion on the eastern branch, creating a basin that localized deposition and preservation of the Aeropuerto Formation (Fig. 2). The Aeropuerto Formation is Late Jurassic to Early Cretaceous in age and is in part the same age as the Cerro del Pingo Complex exposed east of the eastern branch, implying a component of east-side-up slip. However, kinematic data suggest mostly strike-slip motion with a component of east-side-down motion on the eastern branch. It is possible that emplacement of the Cerro del Pingo Complex was initially associated with an east-side-up component of shear along the eastern branch, similar to relationships documented in the Las Tazas pluton further south (Grocott and Taylor 2002), and record of this motion has been largely overprinted by sinistral shear.

The magnitude of dip-slip motion is <2 km based on the shallow rake of slickenlines plunging both north and south across the main branches of the El Salado segment.

Discussion

Correlation of synkinematic plutons and mylonite zones

Based on mineralogical, textural, geochemical and geochronological evidence, we suggest four localities can be correlated across the eastern branch of the AFS to represent two distinct associations of metasedimentary mylonites and synkinematic plutons: the strained c. 134-132 Ma Cerro del Pingo Complex and strained c. 120-119 Ma Cerro del Pingo tonalite (Fig. 13). The two exposures of the older phase of the Cerro del Pingo Complex are both fresh, medium-grained hornblende biotite granodiorite to biotite hornblende tonalite and quartz diorite crosscut by adularia + quartz veinlets (Fig. 4). We note the degree of silicification, adularia + quartz veining, and chloritization of mafic phases is significantly more pronounced in the southern mylonite zone on the western side of the eastern branch. This may be due to fluid exsolution in a slightly higher structural level in the pluton, which would be consistent with a component of east-side-up motion across the eastern branch. Their zircon U-Pb dates (132.6 ± 0.9 Ma and 132.3 ± 1.3 Ma, Seymour *et al.* 2020; 134.0 ± 0.8 Ma, this work, Fig. 6) overlap within error, and both feature variable development of mylonitic fabrics that are concordant with AFS-related brittle fault kinematics, recording synkinematic intrusion during AFS shear. Contact metamorphism is present in the Chañaral Complex metasedimentary rocks that surround the Cerro del Pingo Complex, indicating shallow or epizonal emplacement.

The c. 120 Ma hornblende biotite tonalite described in this study and the c. 119 Ma hornblende biotite tonalite described in Seymour et al. (2020) also have several strong similarities. Both exposures have a similar distribution of Early Cretaceous zircons with cores ranging from c. 137–124 Ma (sample 161-62) and c. 141–123 Ma (sample 161-74), and overgrowths ranging from c. 123–115 Ma (sample 161-62) and c. 122–115 Ma (sample 161-74). We interpret overgrowths to be magmatic in origin based on the presence of oscillatory zoning in CL that truncates internal magmatic textures (Fig. 6). Overgrowths generally have higher absolute concentrations

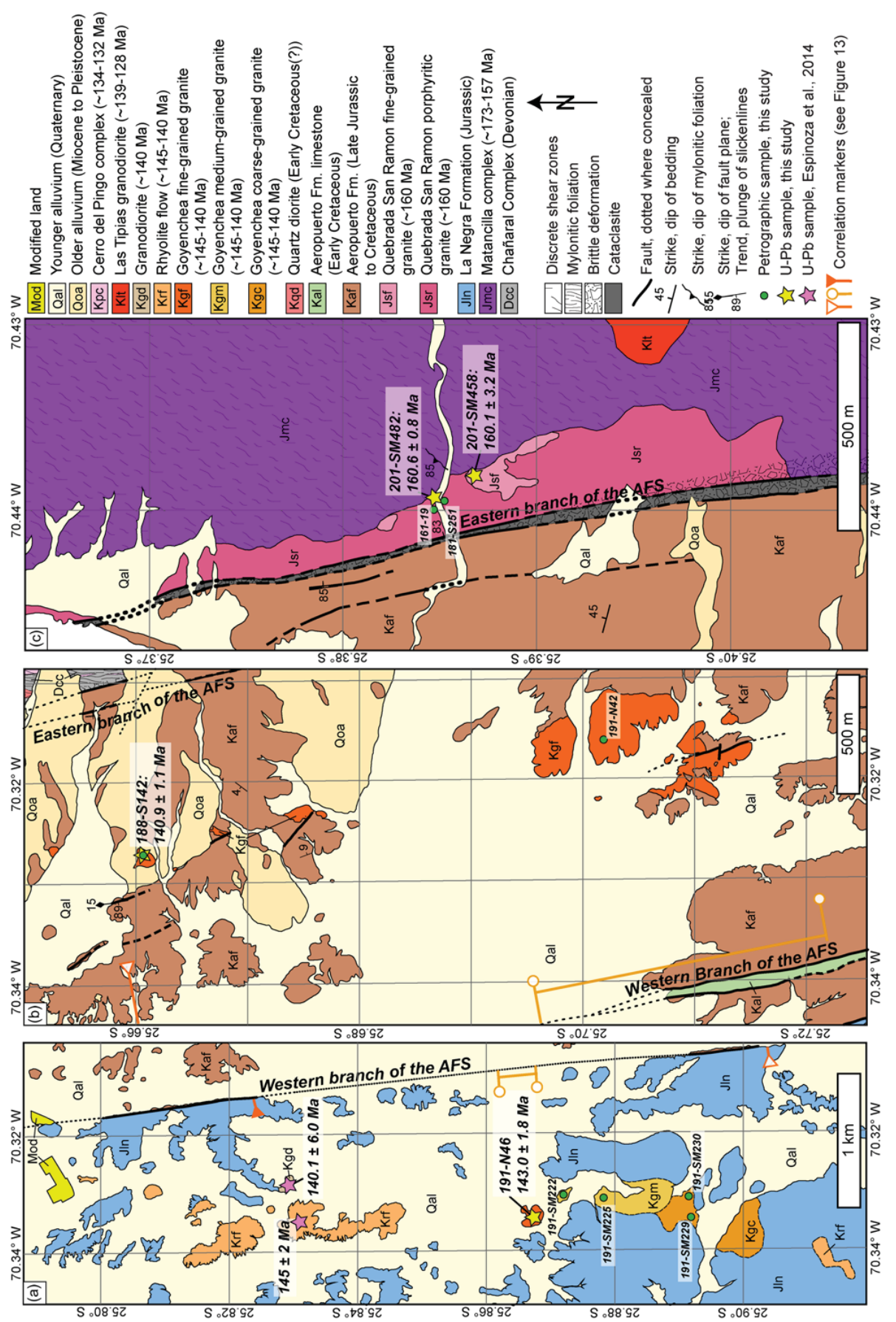


Fig. 9. Inset map of the chain of leucocratic intrusions (a) west of the western branch of the AFS, (b) between the western and eastern branches, and (c) east of the eastern branch. Colours and map symbols are the same as Figure 2. Yellow stars show new U-Pb dates from this study; pink stars show U-Pb dates from Espinoza et al. (2014).

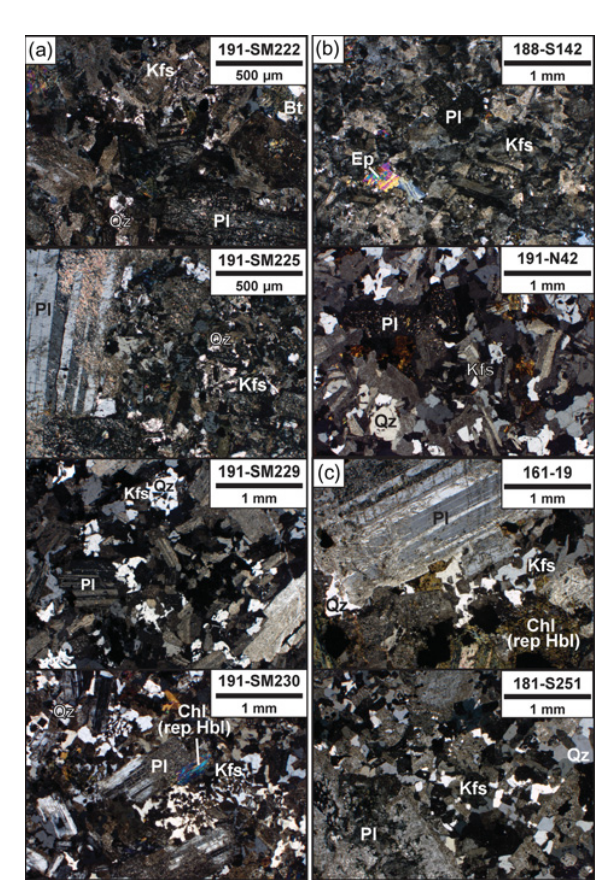


Fig. 10. Photomicrographs in cross-polarized light of the leucocratic igneous bodies in Figure 9 (a) east of the eastern branch, (b) between the eastern and western branches, and (c) west of the western branch. Abbreviations are as follows: Bt = biotite; Chl = chlorite; Kfs = potassium feldspar; Hbl = hornblende; Qz = quartz; Pl = plagioclase; Sa = sanidine; rep = replaced.

of both U and Th than core domains (106-309 ppm in overgrowth v. 49-368 ppm in cores) with individual zircon showing c. 20-180 ppm more U in overgrowths compared to cores (Supplementary File 3); however, the Th/U ratio does not vary significantly between cores (0.44–1.48) and overgrowths (0.28–2.41) and falls within the typical range of igneous zircon (e.g. Kirkland et al. 2015). These lines of evidence rule out a hydrothermal petrogenesis for the overgrowths. The emplacement dates based on magmatic overgrowths overlap within error (118.6 \pm 2.1 Ma, sample 161-62 of Seymour *et al.* 2020; 119.5 \pm 1.8 Ma, sample 161-74, this work, Fig. 6). Results of geochemical analyses show strong similarities between the c. 120–119 Ma tonalites, with whole-rock geochemical analyses that match to within 1.7 wt% for all major oxides (Table 2), and zircon (U-Th)/He cooling dates that overlap within error (Table 1). The development of mylonitic fabrics in the metasedimentary rocks and plutons in both outcrops further indicates the pluton intruded during shear along the AFS. Therefore, we suggest that these tonalite exposures originated as one pluton emplaced c. 120-119 Ma as a younger phase of the Cerro del Pingo Complex, and that the mylonite zones developed in both the c. 134–132 Ma and c. 120–119 Ma phases of the Cerro del Pingo Complex provide information on the magnitude of displacement during Early Cretaceous ductile shear and brittle slip.

The leucocratic intrusions found across the western branch of the El Salado segment are anomalously felsic for the Coastal Cordillera, and have a very distinct mineralogy compared to both the Jurassic (>175 Ma) granodiorites and the Early Cretaceous (<135 Ma)

diorites and tonalites (Figs 4 and 10). The arc-related Jurassic Cerro Concha granodiorite and both phases of the Cerro del Pingo Complex are composed of 15-30% quartz and 0-15% potassium feldspar whereas the leucocratic intrusions are composed of 21-43% quartz and 22-50% potassium feldspar (Fig. 5). Exposures across the western branch include both fine-grained rhyolite and hypabyssal porphyritic intrusions with miarolitic cavities and granophyric textures. Between the western and eastern branches, the intrusions have both miarolitic cavities and spherical bodies filled with fine-grained epidote that together indicate shallow-level (<4 km) emplacement. Fluids exsolved into bubbles from the pluton at this shallow level and crystallized into the fine-grained epidote spheres preserved in the intrusion (e.g. Lowenstern et al. 1997). Epidote is not present within the intrusion outside of these spheres. Textures of the leucocratic granites intruding the La Negra Formation west of the AFS include fine-grained mixtures of quartz and potassium feldspar with quartz and sanidine phenocrysts to porphyritic intrusions with 2-9 mm sericitized plagioclase crystals surrounded by interlocking grains of 1-2 mm potassium feldspar and quartz with occasional granophyric texture. Granophyric textures represent segregation of the eutectic melt composition and miarolitic cavities indicate intrusion at very shallow levels (<4 km of the surface) that resulted in degassing of volatiles into bubbles and undercooling of the magma (e.g. Lowenstern et al. 1997).

The dates of the felsic bodies on either side of the western branch are very similar to zircon U-Pb dates from Espinoza et al. (2014) on a fresh granodioritic pluton that also intrudes the Aeropuerto Formation (140.1 \pm 6.0 Ma) and a spherulitic rhyolite (145 \pm 2 Ma). Although the dates do not overlap within error, the high MSWD values indicate there is a low probability that these zircons are derived from a single population. This means the weighted mean dates do not necessarily represent the emplacement age of these shallow plutons, as there may be a high degree of incorporation of either antecrysts or xenocrysts from the Aeropuerto Formation wall rock. It is possible that a high degree of xenocryst assimilation is also recorded by the preponderance of c. 160 Ma dates in the leucocratic intrusion on the eastern side of the eastern branch at Quebrada San Ramon. Jurassic dates in the Quebrada San Ramon intrusion overlap with the age of the adjacent Matancilla Complex (c. 173-157 Ma; Escribano et al. 2013). Three younger dates from two grains in sample 201-SM482 (c. 135-132 Ma) overlap with both the age of the nearby Las Tipias granodiorite (c. 139–134 Ma; Escribano et al. 2013, Fig. 2), and the youngest dates recorded in the felsic intrusions to the south across the eastern and western branches (Figs 9 and 11). These anomalously young dates raise the possibility that the majority of grains are ante- or xenocrysts and the true emplacement age of the Quebrada San Ramon intrusion is Early Cretaceous, making it another possible offset marker.

To test whether the leucocratic intrusions described above are sourced from the same population of xenocrystic zircons and could therefore be correlated, we applied the likeness metric, which quantifies the degree of overlap between pairs of zircon age spectra (Satkoski et al. 2013), and the similarity metric, which measures the degree of resemblance between overlapping age spectra (Gehrels 2000). For both of these tests, a value of 1 indicates the samples represent the same population. The Quebrada San Ramon intrusion samples show a high degree of similarity and likeness to each other (0.953 and 0.883, respectively), which is expected because they sample two textural varieties of the same intrusion (all results included in Supplementary File 1). The felsic intrusions exposed across the western branch yielded high values of 0.816 for likeness and 0.920 for similarity (calculated using DetritalPy; Sharman et al. 2018). However, the Quebrada San Ramon intrusion shows significantly lower degrees of likeliness or similarity to the felsic intrusions across the western branch (0.715-0.788 and 0.393-

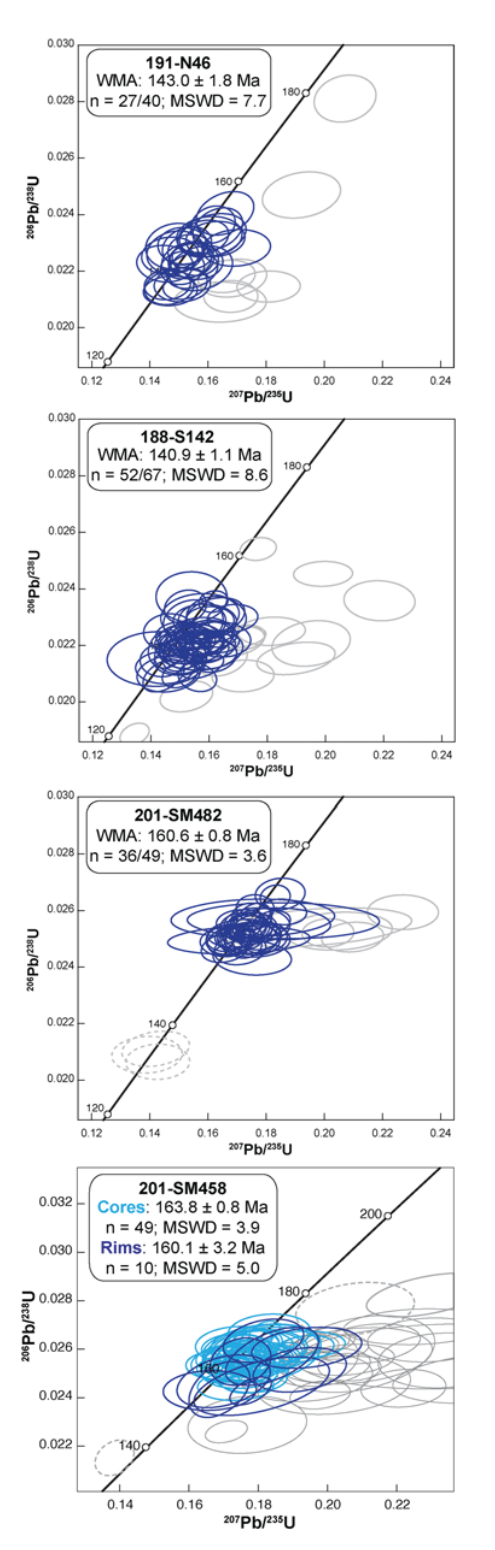


Fig. 11. U–Pb concordia diagrams for the leucocratic intrusions west of the western branch (top, sample 191-N46), between the western and eastern branches (centre, 188-S142), and the Quebrada San Ramon intrusions east of the eastern branch (bottom, 201-SM482 and 201-SM458). Data have been filtered to 10% discordance and grains with >10% discordance are shown in grey. Dashed grey ellipses indicate <10% discordant grains that were rejected from the weighted mean date as outliers. Uncertainties are reported at 2σ.

0.472). Therefore, despite petrographic similarities and the presence of two Early Cretaceous dates in sample 201-SM482, zircon U–Pb data do not support the correlation between the Quebrada San

Ramon intrusion and the other exposures of felsic intrusions. Overall, the high degrees of both likeness and similarity between the U–Pb populations and petrographic analyses between samples 191-N46 and 188-S142 indicate the felsic intrusions between the latitudes of 25.79–25.95°S and 25.65–25.71°S are a part of the same magmatic event. We suggest that the unique composition and texture of the chain of felsic plutons is distinctive enough to provide constraints on the magnitude of slip across the western branch of the El Salado segment.

Zircon (U-Th)/He thermochronometry

The similarity in the range of single-aliquot ZHe dates in lithologies with different U-Pb crystallization dates on either side of the fault points to a shared structural level and/or low-temperature cooling history. Mean ZHe dates and the range of individual aliquots in each sample overlap across the eastern strand of the AFS: the southern Cerro del Pingo has a tightly clustered set of aliquots recording cooling at c. 99 Ma and both exposures of the c. 120-119 Ma tonalite show a range of individual aliquot dates (119.6-85.2 Ma and 107.2-86.8 Ma). As discussed above, the magmatic overgrowths present in the c. 120-119 Ma tonalites have higher [U] than the core domains. Higher U overgrowths can result in excess He being ejected from the grain during the decay process. In these grains, the standard alpha-ejection correction (Farley et al. 1996), which assumes homogenous distribution of U and Th, produces dates that are 'too young' (e.g. Reiners et al. 2004) and can result in errors of up to c. 30% for ejection-corrected ages (Hourigan et al. 2005), resulting significant intrasample variability. In the two c. 120-119 Ma tonalites, individual aliquots show an inverted relationship between date and effective U concentration ([eU], equal to [U] + 0.235[Th]) with younger grains associated with higher [eU]. We therefore attribute the range of individual aliquot dates in these plutons to be a result of parent isotope zonation rather than extended residence time in the partial retention zone.

The c. 6–10 km emplacement depth of the Cerro del Pingo and other Early Cretaceous Coastal Cordillera plutons (Dallmeyer et al. 1996; Kurth 2002) corresponds to the partial retention zone of zircon (160-210°C; Reiners et al. 2002, 2004) in non-magmatic regions with a 25°C km⁻¹ geothermal gradient. However, as shown by Murray et al. (2018), pluton emplacement into the middle crust produces a significant thermal aureole that resets zircon thermochronometers even in the absence of erosion. Our new ZHe dates on the plutons adjacent to the southern mylonite zone overlap with ZHe dates from plutons adjacent to the northern mylonite zone, and in terms of displacement, point to a similar thermal history that allows for the original proximity of these locations (that is, it does not rule out pre-slip proximity of the plutons). These results further show that any correlation of horizontally separated markers across the AFS will represent the majority of slip magnitude and do not reflect a significant component of dip-slip motion across the El Salado segment that would have resulted in different cooling histories on either side of the fault.

Displacement magnitude

Based on the correlation of plutons and the kinematic compatibility of both the mylonitic fabrics and brittle faults, we present a new estimate of the magnitude of slip along the El Salado segment of the AFS. Across the eastern branch, the synkinematic $c.\,120-119$ Ma Cerro del Pingo tonalites are separated by 20.5-26 km and the synkinematic $c.\,134-132$ Ma Cerro del Pingo Complex are separated by 34-38 km (Fig. 13). The $c.\,120-119$ Ma tonalites occur between exposures of the older Cerro del Pingo Complex and, coupled with the development of shear zones in both phases of this Early Cretaceous plutonic complex, indicate that $c.\,8-$

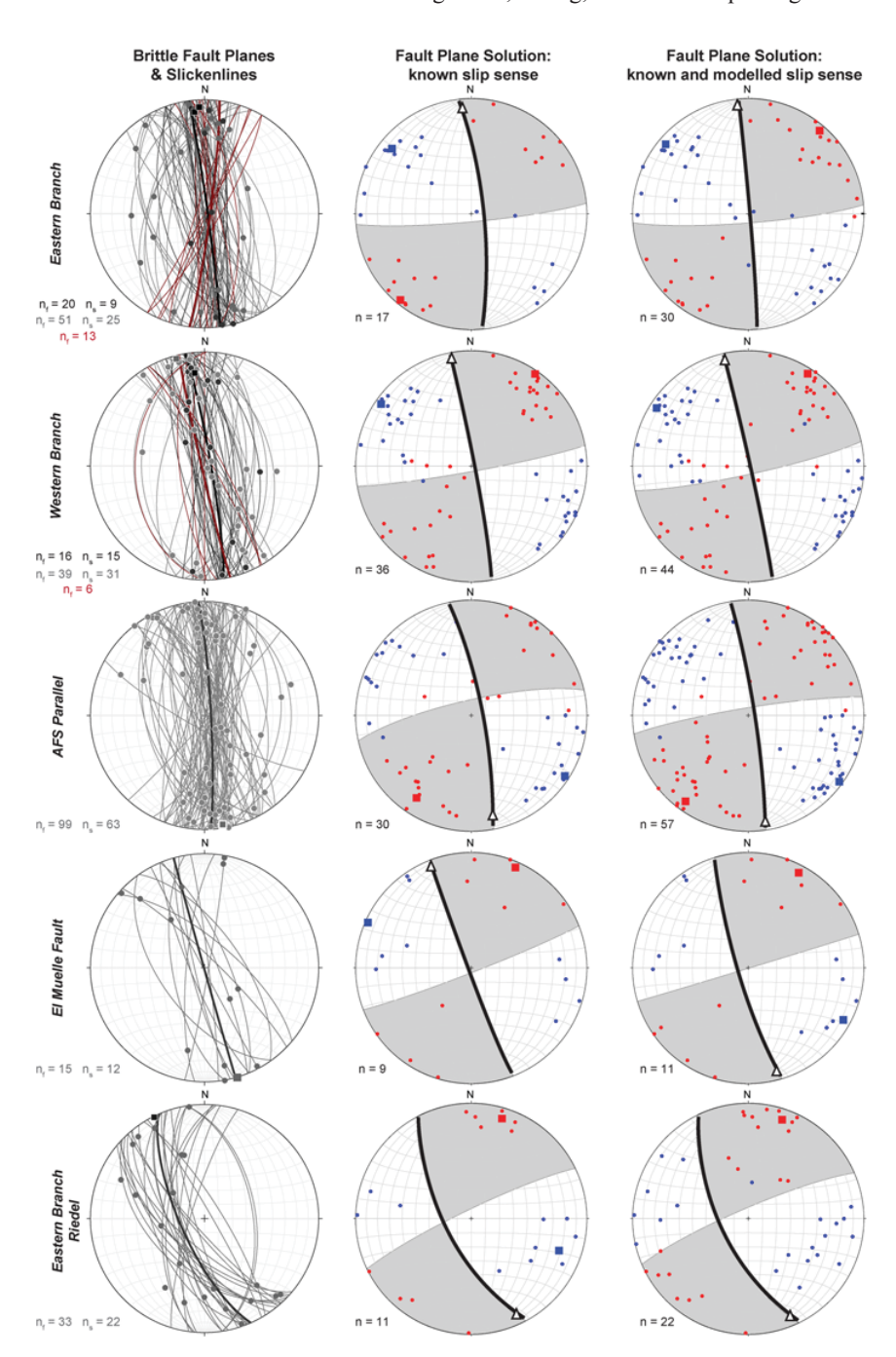


Fig. 12. Equal-area stereograms of brittle faults along the northern El Salado segment. The top row for each fault category shows fault plane measurements (great circles) and slickenline lineation measurements (dots). Principal slip plane measurements for the eastern and western branches are shown in dark grey, faults <50 m from the principal slip plane are shown in light grey, and measurements of foliated gouge in fault cores are shown in maroon. Average measurements are shown in bold and denoted in the corresponding colour to the fault type. The centre column shows P-axes (blue) and T-axes (red) for fault planes with a measured slickenline lineation and an assumed sinistral slip sense, and the right column shows P- and T-axes (blue and red, respectively) for faults with a fielddetermined slip sense only. The fault plane solution is shown as a bold line, the slip vector solution is shown as a bold triangle, and the linked Bingham P- and T-axes are shown by bold squares.

 $17.5~{\rm km}$ of sinistral shear occurred prior to c. $120~{\rm Ma}$. We further note that the two exposures of the prekinematic c. $195~{\rm Ma}$ Cerro Concha plutons are sinistrally separated by $11-15~{\rm km}$ of slip along a subsidiary, NW-trending splay of the eastern branch. The lower magnitude of sinistral separation combined with the lack of mylonitic shear zones developed in the Cerro Concha granodiorite suggests the eastern branch does not record a prior Jurassic history of slip, as we would expect the sinistral separation of Jurassic plutons to exceed the sinistral separation of Early Cretaceous plutons if there had been a protracted pre-Cretaceous slip history. The higher degree of alteration in the exposure of the Cerro Concha on the western side of the splay may represent a higher structural level of the pluton, indicating a degree of east-side-up motion on the fault.

The displacement estimate determined from the leucocratic plutons across the western branch of the AFS is not as clear as the correlation of the Cerro del Pingo Complex and associated metasedimentary mylonites across the eastern branch due to textural variations in the intrusions, occurrence of the leucocratic plutons in a chain rather than a single intrusion, lack of direct interaction between the leucocratic plutons and the eastern branch, and extensive alluvial cover. Textural observations described above suggest that leucocratic granites intruded as a continuous chain of epizonal and hypabyssal plutons along a 190-195° trend. Restoring the separation of the linear trend of these intrusions results in a minimum sinistral separation of c. 6 km whereas restoring the intrusions to a single side-by-side block results in a maximum sinistral separation of c. 29 ± 2 km across the western branch. Restoring offset based on correlation of similar textural domains such as the presence of granophyric textures results in a sinistral separation of c. 16–20 km (Fig. 13). As both sets of leucocratic lithologies show a north-south progression from fine-grained intergrowths of quartz and potassium

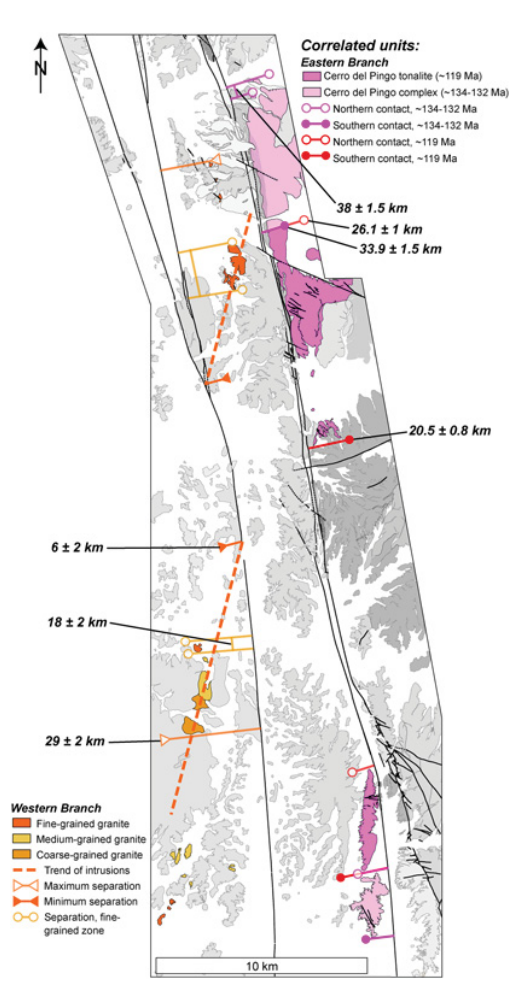


Fig. 13. Correlation of offset markers along the AFS. Pink bars show the 34-38 km sinistral separation of the northern (open circle) and southern (filled circle) contacts of the c. 134-132 Ma Cerro del Pingo Complex and red bars show the 20.5-26 km sinistral separation of the northern (open circle) and southern (filled circle) contacts of the c. 120-119 Ma tonalites. Orange bars show the maximum (c. 29 km, open triangles) and minimum (c. 6 km, filled triangles) separation of leucocratic intrusions across the western branch. Open circles show the 16-20 km of sinistral separation of fine-grained and medium-grained textural zones within the leucocratic intrusions. Paired bars joined by a solid line denote uncertainty in correlation points. Note units not correlated across the AFS are shown in grey and at 50% opacity.

feldspar with c. 2–3 mm crystals of quartz and sanidine to coarser porphyritic plagioclase surrounded by interlocking 1–2 mm quartz and feldspar with granophyric textures, we prefer to correlate textural domains as a horizontal separation marker.

The Quebrada San Ramon granite exposed near the coastline east of the eastern branch is sinistrally separated by $c.\,20$ –30 km from the exposure of leucocratic intrusions with similar textures across the eastern branch (Fig. 9). However, despite the petrographic similarities between these lithologies, our zircon U–Pb data show significant differences between crystallization date and potential sources of xenocrystic zircon and do not support the correlation of the Quebrada San Ramon granite to the felsic intrusions exposed across the western branch. Furthermore, the $c.\,20$ –30 km sinistral separation between the Quebrada San Ramon granite and the leucocratic intrusions between the eastern and western branch is less than the estimated $c.\,34$ –38 km sinistral displacement of the $c.\,134$ –132 Ma Cerro del Pingo Complex, which is better supported by geochronology and field relationships.

Altogether, our data provide a displacement magnitude of c. 54 \pm 6 km for slip on both branches of the El Salado segment between c. 133 and 110 Ma (Figs 13 and 14). We did not identify any other offset markers along the c. 70 km mapped length of the northern El Salado segment. The displacement magnitude across the eastern branch is similar to the Hervé (1987b) estimate of c. 34 km on the Izcuña fault, one of the major branches of the Paposo segment.

Timing and rate of slip

Field relationships provide key insights into the timing of AFS slip. Jurassic plutons along the El Salado segment mapped here do not show evidence for ductile deformation and are prekinematic with respect to AFS sinistral shear (Seymour et al. 2020). Mylonitic tonalites bracket the onset of ductile deformation along the El Salado segment. The oldest pluton to record ductile deformation in the Taltal area is the c. 134-132 Ma Cerro del Pingo Plutonic Complex. Metasedimentary rocks that are spatially associated with this phase of the Cerro del Pingo Complex have undergone contact metamorphism but are undeformed where they are not adjacent to the AFS, and record increasing ductile strain with proximity to the eastern branch of the AFS. Strain in the metasedimentary rocks is concentrated in phyllitic layers along the margins of the Cerro del Pingo Complex, and both phyllitic layers and quartz-rich, micapoor beds are penetratively strained near the center of the Cerro del Pingo Complex. This spatial relationship between mylonites and the Cerro del Pingo Complex indicates sinistral shear along the AFS had initiated by c. 134-132 Ma (Seymour et al. 2020). An Early Cretaceous onset of deformation agrees with previous work by Taylor et al. (1998) and Grocott and Taylor (2002) that documents the coeval initiation of the eastern branch and emplacement of Las Tazas pluton along the central El Salado segment at c. 132 Ma.

Intrusion of the c. 120–119 Ma tonalite between the exposures of the c. 134–132 Ma plutons and the development of high-strain mylonite zones within the tonalites indicate the heat from sustained intrusions of the Cerro del Pingo Complex elevated the geothermal gradient high enough to allow for ductile deformation (Seymour et al. 2020). The metasedimentary rocks spatially associated with both the c. 120–119 Ma tonalite and AFS are highly strained in both phyllitic and quartz-rich layers, with both lithologies forming mylonites, indicating temperatures must have been in excess of the quartz brittle-plastic transition for strike-slip regimes (c. 280-310°C; Stöckhert et al. 1999; Stipp et al. 2002). Cooling of the Cerro del Pingo Complex east of the eastern branch through 310-345°C is recorded by c. 130-129 Ma biotite ${}^{40}\text{Ar}/{}^{39}\text{Ar}$ dates (Espinoza et al. 2014) indicating elevated temperatures that produced ductile deformation are directly tied to pluton emplacement, and the duration of mylonitic deformation along the eastern branch occurred over a relatively short time interval (c. 3–4 Myr). If the mapped c. 8–17.5 km of sinistral separation determined from restoring the northern and southern contacts of the c. 134–132 Ma plutons and c. 120–119 Ma tonalite occurred at a constant rate of c. 0.5-1.5 km Myr⁻¹, then c. 3-4 Myr of mylonitic shearing would produce 1.5-6 km of sinistral displacement, and the remaining c. 6.5-11.5 km of separation would have occurred in the brittle regime. A separate, time-independent estimate of displacement accommodated by mylonitic shearing overlaps with the estimate derived from cooling dates: assuming simple shear across the c. 500–800 m wide shear zone constrained by our mapping, the angle between the average mylonitic foliation and the average orientation of the brittle eastern branch (c. 10-14°, Figs 3 and 6) records the average shear strain ($\gamma = 3.8-5.5$; e.g. Ramsay 1980). This shear strain corresponds to c. 1.9-4.4 km of sinistral displacement across the 500-800 m wide zone in the ductile regime. A component of

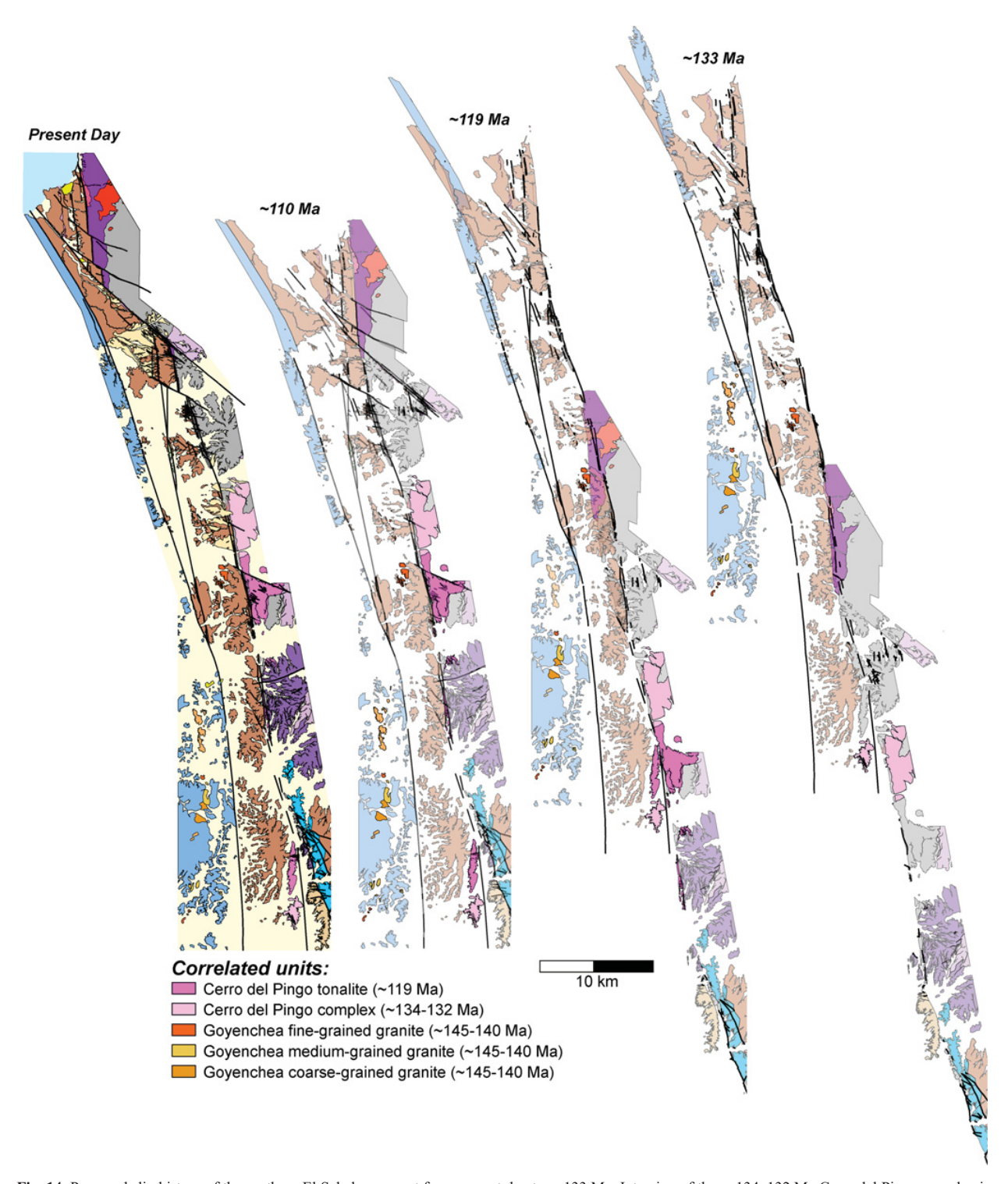


Fig. 14. Proposed slip history of the northern El Salado segment from present day to *c*. 133 Ma. Intrusion of the *c*. 134–132 Ma Cerro del Pingo complex is coeval with the development of metasedimentary mylonites in the Chañaral Complex, recording the initiation of AFS-related strain (far right). Intrusion of the *c*. 120–119 Ma tonalite (centre right) records ongoing strain and the development of additional metasedimentary mylonites along the eastern branch of the El Salado segment. AFS-related deformation ends and motion along the Taltal fault system initiates at *c*. 110 Ma (centre left; see Mavor *et al*. 2020), resulting in the present-day geometry of the El Salado segment (far left) See the Supplementary Plate for a 1: 100 000-scale version.

pure shear across the mylonite zone would reduce the magnitude of sinistral displacement accommodated by ductile shearing. The presence of mylonites and a brittle fault core associated with the c. 120–119 Ma tonalites indicates a second punctuated period of mylonitic deformation that transitioned from ductile shear to brittle slip as the plutons cooled. Cooling through 180°C in both the Cerro

Concha granodiorite and the two phases of the Cerro del Pingo Complex occurred at 108–99 Ma (Seymour *et al.* 2020; this work), indicating the entire duration of ductile and brittle AFS slip at the exposed structural levels occurred at temperatures >180° C.

Several dikes constrain the latest stages of slip along the brittle AFS. The end of AFS slip is recorded by a $10\,\mathrm{m}$ wide and esitic dike

that clearly cuts across most strands of the main eastern branch of the AFS and is sinistrally offset c. 148 m along a fault parallel to the eastern AFS branch (Mavor et al. 2020; Seymour et al. 2020). Interpretation of the age of this latest-synkinematic dike (c. 109.9 \pm 4.0 Ma, Seymour et al. 2020) is complicated by low zircon yield and a significant spread in single grain dates, but can be used to document the ending stages of AFS slip at 114-105 Ma. This timing is corroborated by a dacitic dike located c. 25.5°S that cuts cataclasite of the AFS and has a zircon (U-Th)/He cooling date of 106.7 \pm 8.5 Ma (Mayor et al. 2020), further supporting that brittle slip and the development of AFS-related cataclasite had ceased by the end of the Early Cretaceous. The c. 110 Ma andesitic dike, c. 107 Ma dacitic dike, and brittle faults of the AFS are cut by NW-striking sinistral faults parallel to the younger TFS (Mavor et al. 2020). Based on the spatial offsets discussed above, we can couple these timing estimates with displacement magnitudes to calculate slip rates along the El Salado segment. We suggest that the entire c. 48.5–59.5 km of slip along the El Salado segment occurred over the c. 23 Myr period between c. 133–110 Ma, resulting in a time-averaged slip rate of c. 2.1–2.6 km Myr⁻¹ across the entire northern El Salado segment. The slip rates for each branch are c. 1.5–1.7 km Myr⁻¹ for c. 34–38 km of displacement along the eastern branch and c. 0.7–1.2 km Myr⁻¹ for c. 16-20 km of displacement along the western branch. Expanding this to the maximum allowable range of correlation point separation (38– 70 km) and uncertainty on timing derived from the emplacement of the Cerro del Pingo Complex (± 2 Myr) and latest kinematic dikes (± 4 Myr) produces a maximum range of c. 1.3–4.0 km Myr⁻¹ (entire El Salado segment), c. 1.1-2.3 km Myr⁻¹ (eastern branch), and c. 0.2-1.7 km Myr⁻¹ (western branch).

Fault scaling relationships and comparison to other fault systems

Typical fault displacement:length (d_{max}/L) scaling relationships predict displacement magnitude will be ≤10% of the fault length (Kim and Sanderson 2005). Our documented displacement magnitudes of c. 34-38 km along the c. 180 km eastern branch (maximum $d_{\text{max}}/L = 0.19-0.21$; maximum range 0.18-0.22) and c. 16–20 km along the c. 130 km western branch (maximum $d_{\rm max}/\!L$ = 0.12-0.15; maximum range 0.05-0.22) are consistent with large strike-slip faults reported by MacMillian (1975) and other large displacement faults (Nicol et al. 2020). We note that our d_{max}/L values are likely overestimated because the true lengths of the fault segments are incompletely known given that the north end goes offshore and the southern ends are not precisely located. Our d_{max}/L values exceed the predicted values based on the relationship established for smaller displacement (<220 m displacement) faults along the AFS by Stanton-Yonge et al. (2020); however, higher displacement faults often record higher d_{max}/L than smaller displacement faults (e.g. Nicol et al. 2020 and references therein).

Ratios of $d_{\rm max}/L$ are often high for interacting segments and linked faults (Kim and Sanderson 2005). The fault segments that evolve without obvious connection – termed soft linkage by Walsh and Watterson (1991) – may build up displacement with restricted propagation through the interaction with adjacent faults, producing higher $d_{\rm max}/L$ ratios (e.g. Willemse 1997), while hard linkages produce a drop in $d_{\rm max}/L$ as the fault length abruptly increases while displacement remains the same. The highly segmented nature of the El Salado segment with two major fault branches each individually comprised of more than one fault strand suggests it is a soft-linked system. Soft linkage is a possible result of fault segment nucleation along the margins of Early Cretaceous plutons due to thermal weakening of the crust (Seymour *et al.* 2020), during which time fault length may have been rapidly established in the thermal

aureoles of the plutons and stabilized as the individual branches began to interact, limiting continued fault tip propagation while displacement continued to accumulate (e.g. Walsh *et al.* 2002). A transition from soft to hard linkage is expected for mature fault systems (Peacock and Sanderson 1996) and, in some areas, the El Salado segment developed hard linkages between individual fault strands, such as the NW-striking fault that hosts the Mantoverde iron oxide–copper–gold deposit (Vila *et al.* 1996).

Slip rates of c. $2.1-2.6 \text{ km Myr}^{-1}$ (equivalent to mm yr⁻¹) for the El Salado segment are low compared to modern intra-arc systems: the c. 1200 km Liquiñe-Ofqui fault of southern Chile has modern slip rates of 6.5 mm yr⁻¹ (Wang et al. 2007), the c. 1650 km long Sumatran fault has slip rates c. 15–16 mm yr⁻¹ (Bradley et al. 2017), the c. 300 km Median Tectonic Line has strike-slip rates of 0.8–9.1 mm yr⁻¹, depending on the location along the fault system (Tsutsumi and Okada 1996; Goto 2018), and the c. 1250 km Philippine fault has strike-slip rates ranging from 7.7–31.4 mm yr on individual fault branches (Hsu et al. 2016). The Liquiñe-Ofqui and Sumatran faults are hard-linked systems with major throughgoing faults mapped along the entire length of the arc, and the Philippine fault is a complex system comprised of several interacting, hard-linked strands with differing slip rates. However, geodetically derived slip rates on modern major structures are based on less than a century of data and exclusively sample short-term (earthquake) timescales. The higher slip rates recorded by geodesy may therefore reflect episodic displacement on individual faults interspersed with periods of quiescence rather than plate-boundary-scale strain rates (Mouslopoulou et al. 2009). Lower displacement rates for faults measured over longer time periods are a common phenomenon (e.g. Mouslopoulou et al. 2009) and may be the tectonic equivalent of the 'Sadler Effect' for sedimentation rates (Sadler 1981). Slip rates can vary by up to three orders of magnitude depending on the duration of the sample period and fault length, with higher, more variable short-term (≤20 kyr) slip rates than long-term (<300 kyr) slip rates. Slip rates stabilize over intermediate time scales (>20 kyr to <300 kyr) and record an order of magnitude decrease at timescales greater than 1 Ma as slip rates readjust to tectonic boundary conditions (Mouslopoulou et al. 2009). By taking a long-timeframe approach, our study curbs the potential Sadler Effect bias and captures the relatively uniform rates of long temporal (megayear) or spatial (entire fault system) length scales that may be used to evaluate Mesozoic oblique convergence.

Implications for Mesozoic slip partitioning and plate convergence

Convergence vectors for modern intra-arc faults are well known from geodetic data and the percentage of margin-parallel motion along modern margins can be readily determined. In contrast, the convergence vector across the Early Cretaceous Peru-Chile margin is not as well constrained because most of the Mesozoic oceanic crust in the modern-day Pacific Ocean basin has been subducted. Plate motion reconstructions over the time period of AFS slip suggest Pacific-South America trench-normal convergence of c. 20–50 km Myr⁻¹ and trench-parallel motion of c. 0–20 km Myr⁻¹ between 140 and 110 Ma based on ocean basin seafloor-spreading histories and continental motion anchored to true-polar wandercorrected paleomagnetic data for 200 to 100 Ma (Seton et al. 2012). These plate motion reconstructions result in a convergence obliquity normal to the plate margin that decreased from >60° before 135 Ma to a range of 22-36° between 130 and 110 Ma (Maloney et al. 2013). Additional modeling of the Seton et al. (2012) plate reconstruction data by Butterworth et al. (2016) demonstrates that the obliquity of convergence varied strongly with position along the

margin with proximity to the pole of rotation, and may suggest the pole of rotation of the Phoenix plate shifted at c. 135–130 Ma as subduction progressed. These models as a whole suggest highly oblique subduction along the AFS at c. 130 Ma transitioned to significantly more orthogonal subduction by c. 120 Ma. The opening of a new oceanic ridge to the south of the AFS potentially concurrent with the abandonment of the Pacific–Phoenix ridge in these models at c. 120 Ma produces a period of north-directed oblique convergence followed by a period of relatively orthogonal convergence as the South Atlantic begins to open and South America advanced westward at c. 110 Ma (Seton et al. 2012; Maloney et al. 2013; Butterworth et al. 2016).

Obliquity estimates derived from these reconstructions are comparable to the angles of obliquity and trench-parallel motion rates of modern systems. If this reconstruction is accurate, our estimate of 2.1–2.6 km Myr⁻¹ of slip over that time interval suggests <15% of trench-parallel motion was accommodated along the AFS between 130–110 Ma. In contrast, the 6.5 mm yr⁻¹ of motion along Liquiñe-Ofqui fault system accommodates 30% of the 23-28 mm yr⁻¹ margin-parallel motion across the southern Peru-Chile trench at an angle of c. 20° from normal to the plate boundary (DeMets et al. 1994; Angermann et al. 1999; Kendrick et al. 2003; Wang et al. 2007). At a rate of 15-16 mm yr⁻¹, the Sumatran fault accommodates c. 33-66% of the plate motion between the Sunda and Australian plates along a margin with an obliquity of c. $35-50^{\circ}$ (Tikoff and Teyssier 1994; McCaffrey et al. 2000; Bradley et al. 2017). The Philippine fault is 40-55° from normal to the convergence vector across the Philippine Sea-Sunda plate boundary, and accommodates c. 50% of the margin-parallel motion (Hsu et al. 2016). Finally, the Median Tectonic Line of Japan accommodates c. 25% of the c. 30 mm yr⁻¹ trench-parallel motion across a margin with c. 67° angle between the plate convergence direction and normal to the trench (Loveless and Meade 2010).

This comparison with modern plate margins suggests that the remaining trench-parallel motion across the Mesozoic Peru-Chile margin may have been accommodated either along the slab interface or distributed through the forearc rather than fully concentrating in the magmatic arc, or that significant uncertainties in the modeled relative plate motion vectors remain. It is difficult to evaluate the role of distributed forearc deformation as long-lived subduction erosion has removed both the forearc and the western portion of the Late Jurassic-Early Cretaceous arc following a transition to contraction in the upper plate during the Late Cretaceous (Rutland 1971; Kay and Mahlburg-Kay 1991; Stern 1991; Charrier et al. 2007; Ramos and Folguera 2009; Contreras-Reyes et al. 2014). Uncertainties in the direction and magnitude of relative plate motion are reflected in low degrees of correlation between deformation and major magmatic events in the upper plate and modeled convergence rates and absolute plate motion (Seton et al. 2012; Maloney et al. 2013). While the major elements of the plate reconstruction model described above correlate with the timing of AFS-related shear described here and in Seymour et al. (2020), periods of high magmatic flux such as the development of the Coastal Cordilleran arc do not correlate with subducting slab age, absolute overriding plate velocity, or convergence velocity. High trench-normal (>4 cm yr⁻¹) convergence rates correlate with the development of fold and thrust belts along the Andean margin and may contribute to shortening in the upper plate, but do not uniquely initiate or control the development of high plateaus and fold and thrust belts (Maloney et al. 2013). The lack of correlation between the geologic record of the upper plate and plate motion reconstructions, in conjunction with the need to accommodate an anomalously high proportion of trench-parallel motion outside of a major trench-linked, intra-arc strike-slip fault system, may suggest that the model-derived relative convergence rates do not yet capture the full picture of Mesozoic oblique convergence across the Peru-Chile margin.

Conclusions

Through detailed field mapping and geo/thermochronology, we have identified three pairs of pre-, syn- and post-tectonic intrusions that document the timing, magnitude and rate of slip along two major branches the El Salado segment of the Atacama fault system during Early Cretaceous convergence:

- (1) Two mylonite zones featuring the c. 134–132 Ma Cerro del Pingo Complex and surrounding Chañaral Complex metasedimentary rocks are sinistrally separated across the eastern branch by c. 34–38 km.
- (2) Two additional mylonite zones composed of Chañaral Complex metasedimentary rocks and a c. 120–119 Ma tonalite that intrudes the c. 134–132 Ma Cerro del Pingo Complex are sinistrally separated across the eastern branch by c. 20.5–26 km.
- (3) A chain of leucocratic felsic igneous bodies across the western branch of the El Salado segment are sinistrally separated by c. 6–29 km and likely c. 16–20 km based on restoration of textural domains.

Fault data along the eastern and western branch document dominantly sinistral motion on a subvertical north-striking fault. Crosscutting relationships document c. 23 Myr of deformation between c. 133 and 110 Ma, beginning with the intrusion of the c. 134–132 Ma Cerro del Pingo Complex and ending at c. 110 Ma as a latest-synkinematic dike intruded and was offset by c. 148 m along the eastern branch. These data together with offset markers yield a slip rate of c. 1.5–1.7 km Myr^{-1} across the eastern branch and c. 0.7–1.2 km Myr^{-1} across the western branch, assuming the latter was active over the same time period as the former. The northern El Salado segment as a whole was active at an average rate of c. 2.1–2.6 km Myr⁻¹, resulting in c. 54 \pm 6 km of sinistral displacement. Together our data suggest that sinistral slip along the El Salado segment accounts for <15% of modeled trench-parallel motion during Mesozoic oblique convergence across the Peru-Chile trench, and implies (1) the vast majority of lateral slip was accommodated along the slab interface or distributed through the forearc, or (2) plate convergence rates/obliquity were significantly lower than previously modeled.

Acknowledgements The authors would like to thank R. Ruthven and E. Strickland for field assistance, R. Chatterjee, D. Patterson, and L. Stockli for laboratory assistance at UT-Chron, and Y. Kuiper and J. Ridley for fruitful discussions. Thoughtful reviews from A. Nichol and an anonymous reviewer improved this manuscript. Funding from National Science Foundation Grant #1822064 and a Geological Society of America Student Research Grant supported this work. All geo/thermochronometric data will be made available through the Geochron database upon acceptance of this manuscript.

Author contributions NMS: data curation (lead), formal analysis (lead), investigation (lead), methodology (lead), visualization (lead), writing – original draft (lead), writing – review & editing (lead); JSS: conceptualization (lead), funding acquisition (lead), investigation (equal), methodology (equal), project administration (lead), resources (lead), supervision (lead), writing – original draft (equal), writing – review & editing (equal); RG: investigation (supporting), resources (supporting), visualization (supporting), writing – review & editing (supporting), writing (supporting); SPM: investigation (supporting), visualization (supporting), writing – review & editing (supporting); GA: project administration (supporting), resources (supporting); DFS: data curation (supporting), formal analysis (supporting), methodology (supporting), resources (supporting), validation (supporting), methodology (supporting), resources (supporting), validation (supporting)

Funding This work was funded by the National Science Foundation (1822064) to JSS and Geological Society of America.

Data availability All data generated or analysed during this study are included in this published article (and its supplementary information files).

Scientific editing by Giovanni Camanni

References

- Allmendinger, R.W. and González, G. 2010. Invited review paper: Neogene to Quaternary tectonics of the coastal Cordillera, northern Chile. *Tectonophysics*, 495, 93–110. https://doi.org/10.1016/j.tecto.2009.04.019
- Allmendinger, R.W., Cardozo, N. and Fisher, D.M. 2011. Structural Geology Algorithms: Vectors and tensors. Cambridge University Press.
- Álvarez, J., Jorquera, R., Miralles, C., Padel, M. and Martinez, P. 2016. *Cartas Punta Posallaves y Sierra Vicuña Mackenna, Región de Antofagasta*. Servicio Nacional de Geología y Minería. Carta Geológica de Chile, Geología Básica (1:100.000).
- Angermann, D., Klotz, J. and Reigber, C. 1999. Space-geodetic estimation of the Nazca–South America Euler vector. *Earth and Planetary Science Letters*, 171, 329–334, https://doi.org/10.1016/S0012-821X(99)00173-9
- Arabasz, W.J. 1968. Geologic structure of the Taltal Area, Northern Chile, in relation to the earthquake of December 28, 1966. Bulletin of the Seismological Society of America, 58, 835–842.
- Arabasz, W.J. 1971. Geological and Geophysical Studies of the Atacama Fault Zone in Northern Chile. PhD thesis, California Institute of Technology.
- Arévalo, C. 1995. *Mapa Geológico de la Hoja Los Loros*. Servicio Nacional de Geología y Minería, Documentos de Trabajo, No. 6 (1:100.000).
- Arévalo, C. 2005. Carta Copiapó, Región de Atacama. Servicio Nacional de Geología y Minería. Carta Geológica de Chile, Serie Geología Básica, 91, 54
- Arévalo, C. and Welkner, D. 2008. Geología del área de Carrizal Bajo-Chacritas, Región de Atacama. Servicio Nacional de Geología y Minería, Carta Geológica de Chile, Serie Geología Básica (1:100.000).
- Arévalo, V., Mourgues, O., Amaro, F. and Chávez, M. 2009. Geología del área Vallenar-Domeyko, Región de Atacama. Servicio Nacional de Geología y Minería, Carta Geológica de Chile, Serie Geología Básica (1:100.000).
- Beck Jr, M.E. 1983. On the mechanism of tectonic transport in zones of oblique subduction. *Tectonophysics*, 93, 1–11, https://doi.org/10.1016/0040-1951(83) 90230-5
- Blanco, N., Godoy, E. and Marquardt, C. 2003. Cartas Castilla y Totoral Bajo, Región de Atacama. Servicio Nacional de Geología y Minería. Serie Geología Básica, 77 (1:100.000).
- Bradley, K. E., Feng, L., Hill, E. M., Natawidjaja, D. H. and Sieh, K. 2017. Implications of the diffuse deformation of the Indian Ocean lithosphere for slip partitioning of oblique plate convergence in Sumatra. *Journal of Geophysical Research:Solid Earth*, 122, 572–591, https://doi.org/10.1002/ 2016/JB013549
- Brown, M., Diáz, F. and Grocott, J. 1993. Displacement history of the Atacama fault system 25°00′S–27°00′S, northern Chile. *Geological Society of America Bulletin*, 105, 1165–1174, https://doi.org/10.1130/0016-7606(1993) 105<1165:DHOTAF>2.3.CO:2
- Butterworth, N., Steinberg, D., Müller, R.D., Williams, S., Merdith, A.S. and Hardy, S. 2016. Tectonic environments of South American porphyry copper magmatism through time revealed by spatiotemporal data mining. *Tectonics*, **35**, 2847–2862, https://doi.org/10.1002/2016TC004289
- Cardozo, N. and Allmendinger, R.W. 2013. Spherical projections with OSXStereonet. Computers & Geosciences, 51, 193–205, https://doi.org/10. 1016/j.cageo.2012.07.021
- Cembrano, J., González, G., Arancibia, G., Ahumada, I., Olivares, V. and Herrera, V. 2005. Fault zone development and strain partitioning in an extensional strike-slip duplex: a case study from the Mesozoic Atacama fault system, Northern Chile. *Tectonophysics*, 400, 105–125, https://doi.org/10. 1016/j.tecto.2005.02.012
- Charrier, R., Pinto, L. and Rodríguez, M.P. 2007. Tectonostratigraphic evolution of the Andean Orogen in Chile. *In*: Moreno, T. and Gibbons, W. (eds) *The Geology of Chile*. The Geological Society, London, 21–114.
- Contreras, J.P., Espinoza, M. et al.. 2013. Carta Cifuncho, Región de Antofagasta y Atacama. Servicio Nacional de Geología y Minería, Carta Geológica de Chile, Serie Geología Básica (1:100.000).
- Contreras-Reyes, E., Becerra, J., Kopp, H., Reichert, C. and Díaz-Naveas, J. 2014. Seismic structure of the north-central Chilean convergent margin: Subduction erosion of a paleomagmatic arc. *Geophysical Research Letters*, 41, 1523–1529, https://doi.org/10.1002/2013GL058729
- Creixell, T., Ortiz, L. and Arévalo, V. 2012. Geología del área Carrizalillo-El Tofo, regiones de Atacama y Coquimbo. Servicio Nacional de Geología y Minería (1:100.000).
- Dallmeyer, R.D., Brown, M., Grocott, J., Taylor, G.K. and Treloar, P.J. 1996. Mesozoic magmatic and tectonic events within the Andean plate boundary zone, 26°-27°30′S, north Chile: constraints from ⁴⁰Ar/³⁹Ar mineral ages. *Journal of Geology*, **105**, 19–40, https://doi.org/10.1086/629799
- DeMets, C., Gordon, R., Argus, D. and Stein, S. 1994. Effect of recent revisions to the geomagnetic reversal time scale on estimates of current plate motions. *Geophysics Research Letters*, 21, 2191–2194, https://doi.org/10.1029/ 94GL02118
- Escribano, J., Martínez, P. et al. 2013. Cartas Bahía Isla Blanca y Taltal, Región de Antofagasta. Servicio Nacional de Geología y Minería. Carta Geológica de Chile. Serie Geología Básica. 164–165 (1:100.000).
- Espinoza, M., Contreras, J.P., Jorquera, R., De La Cruz, R., Kraus, S., Ramirez, C. and Naranjo, J. 2014. *Carta Cerro del Pingo, Regiones de Antofagasta y Atacama*. Servicio Nacional de Geología y Minería, Carta Geológica de Chile, Serie Geología Básica 169, (1:100.000).

- Farley, K. A., Wolf, R. A. and Silver, L. T. 1996. The effects of long alphastopping distances on (U-Th)/He ages. *Geochimica Et Cosmochimica Acta*, 60, 4223–4229, https://doi.org/10.1016/S0016-7037(96)00193-7
- Fitch, T.J. 1972. Plate convergence, transcurrent faults, and internal deformation adjacent to southeast Asia and the western Pacific. *Journal of Geophysical Research*, 77, 4432–4459, https://doi.org/10.1029/JB077i023p04432
- Gehrels, G.E. 2000. Introduction to detrital zircon studies of Paleozoic and Triassic strata in western Nevada and northern California. Geological Society of America Special Paper, 347, 1–17, https://doi.org/10.1130/0-8137-2347-7 1
- Godoy, E. and Lara, L. 1998. Hojas Chañaral y Diego de Almagro, Región de Atacama. Servicio Nacional de Geología y Minería, Mapas Geológicos, 05-06 (1:100.000).
- Godoy, E. and Lara, L. 1999. Hoja Puerto Flamenco, Región de Atacama. Servicio Nacional de Geología y Minería, Mapas Geológicos, 15 (1:100.000).
- Godoy, E., Marquardt, C. and Blanco, N. 2003. Carta Cifiuncho, Región de Atacama. Servicio Nacional de Geología y Minería, Carta Geológica de Chile, Serie Geología Básica, 76, (1:100.000).
- González, G. and Carrizo, D. 2003. Segmentación, cinemática y cronología relativa de la deformación tardía de la Falla Salar del Carmen, Sistema de Fallas de Atacama (23° 40'S), norte de Chile. Revista Geológica de Chile, 30, 223-244, https://doi.org/10.4067/S0716-02082003000200005
- González, G., Dunai, T., Carrizo, D. and Allmendinger, R. 2006. Young displacements on the Atacama Fault System, northern Chile from field observations and cosmogenic ²¹Ne concentrations. *Tectonics*, 25, TC3006, https://doi.org/10.1029/2005TC001846
- Goto, H. 2018. Late quaternary slip rates and vectors on the Median Tectonic Line active fault zone in eastern Shikoku, southwest Japan. *Quaternary International*, 471, 267–277, https://doi.org/10.1016/j.quaint.2017.12.013
- Granot, R. and Dyment, J. 2015. The Cretaceous opening of the South Atlantic Ocean. *Earth and Planetary Science Letters*, **414**, 156–163, https://doi.org/10. 1016/j.epsl.2015.01.015
- Grocott, J. and Taylor, G.K. 2002. Magmatic arc fault systems, deformation portioning, and emplacement of granitic complexes in the Coastal Cordillera, northern Chilean Andes (25°30'S to 27°00'S). *Journal of the Geological Society*, **159**, 425–442, https://doi.org/10.1144/0016-764901-124
- Grocott, J., Brown, M., Dallmeyer, R.D., Taylor, G.K. and Treloar, P.J. 1994. Mechanisms of continental growth in extensional arcs: An example from the Andean plate-boundary zone. *Geology*, **22**, 391–394, https://doi.org/10.1130/0091-7613(1994)022<0391:MOCGIE>2.3.CO;2
- Haschke, M., Günther, A., Melnick, D., Echtler, H., Reutter, K.J., Scheuber, E. and Oncken, O. 2006. Central and southern Andean tectonic evolution inferred from arc magmatism. *In*: Oncken, O., Chong, G. *et al.* (eds) *The Andes*. Springer, Berlin, Heidelberg, 337–353.
- Hervé, M. 1987a. Movimiento normal de la falla Paposo, Zona de Falla Atacama, en el Mioceno, Chile. Andean Geology, 31, 31–36, https://doi.org/10.5027/ andgeoV14n2-a04
- Hervé, M. 1987b. Movimiento sinistral en el Cretácico Inferior de la Zona de Falla de Atacama al Norte de Paposo (24°S), Chile. *Andean Geology*, **31**, 37–42
- Hourigan, J.K., Reiners, P.W. and Brandon, M.T. 2005. U-Th zonation-dependent alpha-ejection in (U-Th)/He chronometry. *Geochimica et Cosmochimica Acta*, 69, 3349–3365, https://doi.org/10.1016/j.gca.2005.01.024
- Hsu, Y.J., Yu, S.B. et al. 2016. Interseismic deformation and moment deficit along the Manila subduction zone and the Philippine Fault system, *Journal of Geophysical Research:Solid Earth*, 121, 7639–7665, https://doi.org/10.1002/ 2016/JB013082
- Jaillard, E., Soler, P., Carlier, G. and Mourier, T. 1990. Geodynamic evolution of the northern and central Andes during early to middle Mesozoic times: a Tethyan model. *Journal of the Geological Society, London*, 147, 1009–1022, https://doi.org/10.1144/gsjgs.147.6.1009
- Jarrard R.D. 1986. Terrane motion by strike-slip faulting of forearc slivers. Geology, 14, 780–783, https://doi.org/10.1130/0091-7613(1986)14<780: TMBSFO>2.0.CO;2
- Kay, R.W. and Mahlburg-Kay, S. 1991. Creation and destruction of lower continental crust. Geologische Rundschau, 80, 259–278, https://doi.org/10. 1007/BF01829365
- Kendrick, E., Bevis, M., Smalley, R.J., Brooks, B., Vargas, R.B., Lauría, E. and Fortes, L.P.S. 2003. The Nazca—South America Euler vector and its rate of change. *Journal of South American Earth Sciences*, 16, 125–131, https://doi. org/10.1016/S0895-9811(03)00028-2
- Kim, Y.S. and Sanderson, D.J. 2005. The relationship between displacement and length of faults: a review. *Earth-Science Reviews*, 68, 317–334, https://doi.org/ 10.1016/j.earscirev.2004.06.003
- Kirkland, C.L., Smithies, R.H., Taylor, R.J.M., Evans, N. and McDonald, B. 2015. Zircon Th/U ratios in magmatic environs. *Lithos*, 212, 397–414, https://doi.org/10.1016/j.lithos.2014.11.021
- Kirsch, M., Paterson, S.R., Wobbe, F., Ardila, A.M.M., Clausen, B.L. and Alasino, P.H. 2016. Temporal histories of Cordilleran continental arcs: Testing models for magmatic episodicity. *American Mineralogist*, 101, 2133–2154, https://doi.org/10.2138/am-2016-5718
- Kurth, D. 2002. Die Nordchilenische K\u00fcstenkordillere bei Taltal: Scherzonen und forearc-sliver im Jurassischen und Unterkretazischen magmatischen Bogen: ein Verfahren zur Lautheitsskalierung bei Kindern. PhD thesis, Frieie Universitat Berlin.

- Lara, L. and Godoy, E. 1998. Hoja Quebrada Salitrosa, Región de Atacama. Servicio Nacional de Geología y Minera, Manas Geológicos, 4 (1:100.000).
- Loveless, J. and Meade, B. 2010. Geodetic imaging of plate motions, slip rates, and partitioning of deformation in Japan. *Journal of Geophysical Research*, 115, B02410, https://doi.org/10.1029/2008JB006248
- Lowenstern, J.B., Clynne M.A. and Bullen T.D. 1997. Comagmatic A-Type Granophyre and Rhyolite from the Alid Volcanic Center, Eritrea, Northeast Africa. *Journal of Petrology*, 38, 1707–1721, https://doi.org/10.1093/petroj/ 38.12.1707
- Ludwig, K. 2003. ISOPLOT 3.00: A Geochronology Toolkit for Microsoft Excel.
 Berkeley Geochronological Center Special Publication, Berkeley, California.
 MacMillian, R.A. 1975. The Orientation and Sense of Displacement of Strike-Slip Faults in Continental Crust. BS thesis, Carelton University.
- Maloney, K.T., Clarke, G.L., Klepeis, K.A. and Quevedo, L. 2013. The Late Jurassic to present evolution of the Andean margin: Drivers and the geological record. *Tectonics*, 32, 1049–1065, https://doi.org/10.1002/tect.20067
- Marrett, R. and Allmendinger, R.W. 1990. Kinematic analysis of fault-slip data. Journal of Structural Geology, 12, 973–986, https://doi.org/10.1016/0191-8141(90)90093-E
- Marsh, J.H. and Stockli, D.F. 2015. Zircon U–Pb and trace element zoning characteristics in an anatectic granulite domain: Insights from LASS-ICP-MS depth profiling. *Lithos*, 239, 170–185, https://doi.org/10.1016/j.lithos.2015. 10.017
- Matthews, K.J., Seton, M. and Müller, R.D. 2012. A global-scale plate reorganization event at 105 – 100 Ma. Earth and Planetary Science Letters, 355, 283–298, https://doi.org/10.1016/j.epsl.2012.08.023
- Mavor, S.P., Singleton, J.S. et al.. 2020. Timing, kinematics, and displacement of the Taltal fault system, northern Chile: Implications for the Cretaceous tectonic evolution of the Andean margin, *Tectonics*, 39, https://doi.org/10.1029/ 2019TC005832
- McCaffrey, R., Zwick, P. et al. 2000. Strain partitioning during oblique plate convergence in northern Sumatra: geodetic and seismologic constraints and numerical modeling. *Journal of Geophysical Research*, 105, 28,363–28,376, https://doi.org/10.1029/1999JB900362
- Mouslopoulou, V., Walsh, J.J. and Nicol, A. 2009. Fault displacement rates on a range of timescales. *Earth and Planetary Science Letters*, 278, 186–197, https://doi.org/10.1016/j.epsl.2008.11.031
- Murray, K.E., Braun, J. and Reiners, P.W. 2018. Toward robust interpretation of low-temperature thermochronometers in magmatic terranes. *Geochemistry*, *Geophysics*, *Geosystems*, 19, 3739–3763, https://doi.org/10.1029/ 2018GC007595
- Naranjo, J.A. and Puig, A. 1984. *Hojas Taltal Y Chañaral*. Servicio Nacional de Geología y Minería, Carta Geológica de Chile, Nos. 62-63, (1:250,000).
- Naranjo, J.A., Hervé, F., Prieto, X. and Munizaga, F. 1984. Actividad Cretácica de la falla Atacama al este de Chañaral: Milonitizadón y plutonismo. Comunicaciones, 34, 57–66.
- Nicol, A., Walsh, J.J., Childs, C. and Manzocchi, T. 2020. The growth of faults. In: Tanner, D. and Brandes, C. (eds) Understanding Faults: Detecting, Dating, and Modelling. Elsevier, 221–256.
- Parada, M.A., López-Escobar, L. et al.. 2007. Andean Magmatism. In: Moreno, T. and Gibbons, W. (eds) The Geology of Chile. The Geological Society, London, 115–146.
- Peacock, D.C.P. and Sanderson, D.J. 1996. Effects of propagation rate on displacement variations along faults. *Journal of Structural Geology*, 18, 311–320, https://doi.org/10.1016/S0191-8141(96)80052-6
- Petit, J.P. 1987. Criteria for the sense of movement on fault surfaces in brittle rocks. *Journal of Structural Geology*, **9**, 597–608, https://doi.org/10.1016/0191-8141(87)90145-3
- Platt, J.P. 1993. Mechanics of oblique convergence. *Journal of Geophysical Research: Solid Earth*, 98, 16239–16256, https://doi.org/10.1029/93JB00888
- Ramos, V.A. and Folguera, A. 2009. Andean flat-slab subduction through time. Geological Society, London, Special Publications, 327, 31–54, https://doi.org/ 10.1144/SP327.3
- Ramsay, J.G. 1980. Shear zone geometry: a review. *Journal of Structural Geology*, **2**, 83–99, https://doi.org/10.1016/0191-8141(80)90038-3
- Reiners, P.W., Farley, K.A. and Hickes, H.J. 2002. He diffusion and (U-Th)/He thermochronometry of zircon: initial results from Fish Canyon Tuff and Gold Butte. *Tectonophysics*, 349, 297–308, https://doi.org/10.1016/S0040-1951 (02)00058-6
- Reiners, P.W., Spell, T., Nicolescu, S. and Zanetti, K. 2004. Zircon (U–Th)/He thermochronometry: He diffusion and comparisons with Ar-40/Ar-39 dating. *Geochimica et Cosmochimica Acta*, 68, 1857–1887, https://doi.org/10.1016/j.gca.2003.10.021
- Ruthven, R.C., Singleton, J.S. et al. 2020. The geometry, kinematics, and timing of deformation along the southern segment of the Paposo fault zone, Atacama fault system, northern Chile. Journal of South American Earth Sciences, 97, https://doi.org/10.1016/j.jsames.2019.102355
- Rutland, R.W.R. 1971. Andean orogeny and ocean floor spreading. *Nature*, 233, 252–255, https://doi.org/10.1038/233252a0
- Sadler, P.M. 1981. Sediment accumulation rates and the completeness of stratigraphic sections. *The Journal of Geology*, 89, 569–584, https://doi.org/ 10.1086/628623
- Satkoski, A.M., Wilkinson, B.H., Hietpas, J. and Samson, S.D. 2013. Likeness among detrital zircon populations-An approach to the comparison of age

- frequency data in time and space. GSA Bulletin, 125, 1783–1799, https://doi.org/10.1130/B30888.1
- Scheuber, E. and Andriessen, P.A.M. 1990. The kinematic and geodynamic significance of the Atacama fault zone, northern Chile. *Journal of Structural Geology*, 12, 243–257, https://doi.org/10.1016/0191-8141(90)90008-M
- Scheuber, E. and González, G. 1999. Tectonics of the Jurassic-Early Cretaceous magmatic arc of the north Chilean Coastal Cordillera (22°-26°S): A story of crustal deformation along a convergent plate boundary. *Tectonics*, **18**, 895–910, https://doi.org/10.1029/1999TC900024
- Scheuber, E., Bogdanic, T., Jensen, A. and Reutter, K.J. 1994. Tectonic development of the north Chilean Andes in relation to plate convergence and magmatism since the Jurassic. *In*: Reutter, K.-J., Scheuber, E. and Wigger, P.J. (eds) *Tectonics of the Southern Central Andes*. Springer Berlin Heidelberg, 121–139.
- Scheuber, E., Hammerschmidt, K. and Friedrich, H. 1995. ⁴⁰Ar/³⁹Ar and Rb-Sr analyses from ductile shear zones from the Atacama Fault Zone, northern Chile: the age of deformation. *Tectonophysics*, **250**, 61–87, https://doi.org/10.1016/0040-1951(95)00044-8
- Schütt, J. M. and Whipp, D. M. 2020. Controls on continental strain partitioning above an oblique subduction zone, Northern Andes. *Tectonics*, 38, https://doi. org/10.1029/2019TC005886
- Seton, M., Müller, R.D. et al.. 2012. Global continental and ocean basin reconstructions since 200 Ma. Earth Science Reviews, 113, 212–270, https://doi.org/10.1016/j.earscirev.2012.03.002 https://doi.org/10.1016/j.earscirev.2012.03.002
- Seymour, N.M., Singleton, J.S., Mavor, S.P., Gomila, R., Stockli, D.F., Heuser, G. and Arancibia, G. 2020. The relationship between arc magmatism and deformation along the intra-arc strike-slip Atacama fault system, northern Chile. *Tectonics*, 39, https://doi.org/10.1029/2019TC005702
- Sharman, G.R., Sharman, J.P. and Sylvester, Z. 2018. detritalPy: A Python-based toolset for visualizing and analysing detrital geo-thermochronologic data. *The Depositional Record*, 4, 202–215, https://doi.org/10.1002/dep2.45
- St. Amand, P. and Allen, C.R. 1960. Strike-slip faulting in northern Chile. Geological Society of America Bulletin, 71, 1965.
- Stanton-Yonge, A., Cembrano, J., Griffith, W.A., Jensen, E. and Mitchell, T.M. 2020. Self-similar length-displacement scaling achieved by scale-dependent growth processes: Evidence from the Atacama Fault System. *Journal of Structural Geology*, 103993, https://doi.org/10.1016/j.jsg.2020.103993
- Stern, C.R. 1991. Role of subduction erosion in the generation of Andean magmas. *Geology*, **19**, 78–81, https://doi.org/10.1130/0091-7613(1991) 019<0078:ROSEIT>2.3.CO:2
- Stipp, M., Stunitz, H., Heilbronner, R. and Schmid, S.M. 2002. The eastern Tonale fault zone: a 'natural laboratory' for crystal plastic deformation of quartz over a temperature range from 250 to 700 C. *Journal of Structural Geology*, 24, 1861–1884, https://doi.org/10.1016/S0191-8141(02)00035-4
- Stöckhert, B., Brix, M.R., Kleinschrodt, R., Hurford, A.J. and Wirth, R. 1999. Thermochronometry and microstructures of quartz—a comparison with experimental flow laws and predictions on the temperature of the brittle– plastic transition. *Journal of Structural Geology*, 21, 351–369, https://doi.org/ 10.1016/S0191-8141(98)00114-X
- Taylor, G.K., Grocott, J., Pope, A. and Randall, D.E. 1998. Mesozoic fault systems, deformation and fault block rotation in the Andean forearc: a crustal scale strike-slip duplex in the Coastal Cordillera of northern Chile. *Tectonophysics*, 299, 93–109, https://doi.org/10.1016/S0040-1951(98)00200-5
- Teyssier, C., Tikoff, B. and Markley, M. 1995. Oblique plate motion and continental tectonics. *Geology*, 23, 447–450, https://doi.org/10.1130/0091-7613(1995)023<0447:OPMACT>2.3.CO;2
- Tikoff, B. and Teyssier, C. 1994. Strain modeling of displacement-field partitioning in transpressional orogens. *Journal of Structural Geology*, 16, 1575–1588, https://doi.org/10.1016/0191-8141(94)90034-5
- Tsutsumi, H. and Okada, A. 1996. Segmentation and Holocene surface faulting on the Median Tectonic Line, southwest Japan. *Journal of Geophysical Research: Solid Earth*, **101**, 5855–5871, https://doi.org/10.1029/95JB01913
- Veloso, E.E., Gomila, R., Cembrano, J., González, R., Jensen, E. and Arancibia, G. 2015. Stress fields recorded on large-scale strike-slip fault systems: Effects on the tectonic evolution of crustal slivers during oblique subduction. *Tectonophysics*, 664, 244–255, https://doi.org/10.1016/j.tecto. 2015.09.022
- Vila, T., Lindsay, N. and Zamora, R. 1996. Geology of the Manto Verde Copper Deposit, northern Chile: A specularite-rich, hydrothermal-tectonic breccia related to the Atacama fault zone. Society of Economic Geologists, Special Publication, 5, 157–170.
- Walsh, J. J. and Watterson, J. 1991. Geometric and kinematic coherence and scale effects in normal fault systems. *In*: Roberts, A.M., Yielding, G. and Freeman, B. (eds) *The Geometry of Normal Faults. Geological Society, London, Special Publications*, 56, 193–203, https://doi.org/10.1144/GSL.SP.1991.056.01.13
- Walsh, J.J., Nicol, A. and Childs, C. 2002. An alternative model for the growth of faults. *Journal of Structural Geology*, 24, 1669–1675, https://doi.org/10.1016/ S0191-8141(01)00165-1
- Wang, K., Hu, Y. et al.. 2007. Crustal motion in the zone of the 1960 Chile earthquake: detangling earthquake-cycle deformation and forearc-silver translation. Geochemistry, Geophyics, Geosystems, 8, 1–14, https://doi.org/ 10.1029/2007GC001721

- Welkner, D., Arévalo, C. and Godoy, E. 2006. *Geología del área Freirina–El Morado, Región de Atacama*. Carta Geológica de Chile, Serie Geología Básica, **44** (1:100.000).
- Willemse, E.J. 1997. Segmented normal faults: Correspondence between threedimensional mechanical models and field data. *Journal of Geophysical Research: Solid Earth*, **102**, 675–692, https://doi.org/10.1029/96JB01651
- Wolfe, M.R. and Stockli, D.F. 2010. Zircon (U-Th)/He thermochronometry in the KTB drill hole, Germany, and its implications for bulk He diffusion kinetics in zircon. *Earth and Planetary Science Letters*, **295**, 69–82, https://doi.org/10.1016/j.epsl.2010.03.025
- Moodcock, N.H. 1986. The role of strike-slip fault systems at plate boundaries.
 Philosophical Transactions of the Royal Society of London, 317, 13–27.